Geomechanical Log Deduced from Porosity and Mineralogical Content

E. Bemer, O. Vincké, P. Longuemare

▶ **To cite this version:**

E. Bemer, O. Vincké, P. Longuemare. Geomechanical Log Deduced from Porosity and Mineralogical Content. Oil & Gas Science and Technology - Revue d'IFP Energies nouvelles, 2004, 59 (4), pp.405-426. 10.2516/ogst:2004028 . hal-02017310

HAL Id: hal-02017310
https://ifp.hal.science/hal-02017310

Submitted on 13 Feb 2019

HAL is a multi-disciplinary open access archive for the deposit and dissemination of scientific research documents, whether they are published or not. The documents may come from teaching and research institutions in France or abroad, or from public or private research centers.

L'archive ouverte pluridisciplinaire **HAL**, est destinée au dépôt et à la diffusion de documents scientifiques de niveau recherche, publiés ou non, émanant des établissements d'enseignement et de recherche français ou étrangers, des laboratoires publics ou privés.

Oil & Gas Science and Technology – Rev. IFP, Vol. 59 (2004), No. 4, pp. 405-426
Copyright © 2004, Institut français du pétrole

Dossier

Interactive Drilling / Forage interactif

Geomechanical Log Deduced from Porosity and Mineralogical Content

E. Bemer[1], O. Vincké[1] and P. Longuemare[1]

1 Institut français du pétrole, 1 et 4, avenue de Bois-Préau, 92852 Rueil-Malmaison Cedex - France
e-mail: elisabeth.bemer@ifp.fr - olivier.vincke@ifp.fr - pascal.longuemare@ifp.fr

Résumé — Diagraphie géomécanique déduite de la porosité et de la composition minéralogique — Le projet de recherche intitulé “diagraphie géomécanique” vise à estimer les propriétés mécaniques des roches à partir d’un ensemble de modèles dont les paramètres d’entrée peuvent être déduits de diagraphies en cours de forage ou de mesures sur échantillons (si certaines sont disponibles). Le point crucial est de s’attacher à définir des modèles relativement généraux et faciles à utiliser. Dans cet article, nous proposons différents modèles analytiques permettant d’estimer les propriétés poroélastiques et de rupture des calcaires et des grès, directement à partir de leur porosité et, uniquement dans le cas des propriétés élastiques des grès, de leur teneur en minéraux. Les propriétés obtenues sont cohérentes avec les données expérimentales.

La seconde étape du projet consistera effectivement à déduire les données d’entrée des modèles (ici la porosité et la teneur en minéraux) de diagraphies en cours de forage et à comparer les résultats obtenus à des essais sur échantillons. Une diagraphie géomécanique pourrait alors être automatiquement générée à partir des diagraphies standard et aider ainsi à optimiser le forage. Nous avons également prévu de tester la même approche sur les propriétés plastiques des roches et le comportement des argiles.

Abstract* — *Geomechanical Log Deduced from Porosity and Mineralogical Content — *The “geomechanical log” research project aims at estimating rock mechanical properties from a set of models, whose input data can be deduced from drilling logs and measurements on core samples (if these are available). The key point is to focus on defining relatively general and easy to handle models. In this paper, we propose various analytical models allowing one to estimate poroelastic and failure properties of limestones and sandstones directly from their porosity and, in the specific case of sandstone poroelastic characteristics, their mineralogical content. The properties obtained are in reasonable agreement with experimental data.*

The second step of the project will be to actually infer the input data for the models (here porosity and mineral content) from drilling logs and to compare the results obtained to tests on core samples. A geomechanical log could then be automatically created from standard logs and help to optimize drilling. We also intend to test the same approaches on rock plastic properties and shale behavior.

NOMENCLATURE

Latin letters

b	Biot's coefficient
c'	cohesion
C'	effective pressure at the onset of shear-induced dilation
C^*	effective pressure at the onset of shear-enhanced compaction
G	shear modulus
K_{fl}	fluid bulk modulus
K_o	drained bulk modulus
K_s	bulk modulus of the solid matrix
m	dimensionless normalization parameter
m^{fl}	fluid mass variation
M	Biot's modulus
$p = -\sigma$	mean pressure
$p' = p - p_p$	Terzaghi's effective mean pressure
p^*	grain crushing and pore collapse pressure
p_c	confining pressure
P_c	effective pressure at the onset of grain crushing and pore collapse
p_p	pore pressure
P_s	effective mean pressure at the peak stress
$q = \sqrt{\frac{3}{2}\underline{\underline{s}}:\underline{\underline{s}}}$ with $\underline{\underline{s}} = \underline{\underline{\sigma}} - \sigma\underline{\underline{1}}$	deviatoric stress
V_b	bulk volume
V_p	pore volume
V_s	solid matrix volume.

Greek letters

$\underline{\underline{\varepsilon}}$	strains
ε_a	axial strain
ε_r	radial strain
$\varepsilon_d = \sqrt{\frac{2}{3}\underline{\underline{e}}:\underline{\underline{e}}}$ with $\underline{\underline{e}} = \underline{\underline{\varepsilon}} - \varepsilon\underline{\underline{1}}$	deviatoric strain
$\varepsilon_v = \mathrm{tr}\,\underline{\underline{\varepsilon}}$	volumetric strain
$\phi = \frac{V_p}{V_b}$	Eulerian porosity
$\Phi = \frac{V_p}{V_b^o}$	Lagrangian porosity
φ'	angle of internal friction
ρ_o^{fl}	fluid density
$\underline{\underline{\sigma}}$	Cauchy's stresses
$\sigma = \frac{\mathrm{tr}\,\underline{\underline{\sigma}}}{3}$	mean stress
$\underline{\underline{\sigma}}' = \underline{\underline{\sigma}} + p_p\,\underline{\underline{1}}$	effective stress of Terzaghi
σ_a	axial stress.

INTRODUCTION

The object of the "geomechanical log" research project is to define software based on a set of models, which will allow rock mechanical properties to be estimated from the porosity, mineral content, etc. Input data for the models will be deduced from drilling logs and core samples (if these are available). The properties sought after are: the poroelastic properties (bulk and shear moduli, Biot's coefficient and Biot's modulus), yield criteria and plastic flow laws, failure criteria (shear failure and cap surface). The predicted rock properties will provide input data for any drilling model, well bore stability software, etc., and could then help to optimize drilling.

The core of the project is to propose models, which are at the same time relatively general, easy to handle, based on a restrained number of parameters accessible from drilling logs and, naturally, which give reasonable estimations of rock mechanical properties. Concessions are thus inevitable. First, we consider four rock classes according to similarity of behavior: cemented sandstones, poorly cemented sandstones, limestones and shales.

Experimental data available in the literature mainly concerns limestones and cemented sandstones. Poorly cemented sandstones are indeed difficult to characterize due to coring and heterogeneity problems. Low permeability of shales and their sensitivity to water complicate the tests by showing a strong effect of the strain rate and the saturating fluid. Literature data on shales thus needs to be handled carefully. From a more pragmatic point of view, cap rocks have been less studied than reservoir rocks and the operators' interest in unconsolidated reservoirs is quite recent.

This paper presents the results of the first step of the project dedicated to the poroelastic and failure properties of limestones and sandstones. Further data will improve the proposed laws. Investigations on plastic properties and shales behavior are in progress.

1 POROELASTIC PROPERTIES

Rock poroelastic behavior is studied within the framework of Biot's mechanics of fluid saturated porous solids under the hypothesis of small perturbations and isothermal transformations (Coussy, 1994; Charlez, 1991). Tensile stress and strain are taken positive.

Consider an isotropic homogeneous porous material saturated with a viscous compressible fluid and submitted to stresses $\underline{\underline{\sigma}}$ and pore pressure p_p. To this stress state corresponds a strain state defined by strains $\underline{\underline{\varepsilon}}$ and variation in fluid mass content m^{fl} (per unit of initial volume). m^{fl} is taken positive for an incoming fluid and can be expressed as (Coussy, 1994):

$$m^{fl} = (1+\varepsilon_v)\rho^{fl}\phi - \rho_o^{fl}\phi_o \qquad (1)$$

where $\phi = V_p/V_b$ is the (Eulerian) porosity, ρ^{fl} is the fluid density, $\varepsilon_v = \mathrm{tr}\,\underline{\underline{\varepsilon}}$ is the volumetric strain and subscript *o* denotes the reference state.

The elastic constitutive law of the saturated porous material can be derived from the behavior of the dry material *(i.e.* without any fluid in the porous space) and the behavior of the matrix (solid and unconnected porosity) (Biot, 1973; Bemer *et al.*, 2001). Biot introduced the concept of semi-linearity, which stipulates that the solid matrix strains depend linearly on stresses and pore pressure, whereas the strains due to the effective stresses ($\underline{\underline{\sigma}}' = \underline{\underline{\sigma}} + p_p\,\underline{\underline{1}}$) involve nonlinear modifications of local geometries, such as changes in contact areas, crack closure, etc. Hence, both in linear and nonlinear poroelasticity, the solid matrix is supposed isotropic and linearly elastic with bulk modulus K_s and shear modulus G_s.

For a linearly elastic material, with drained bulk modulus K_o and shear modulus G, the constitutive law of the saturated porous material is given by:

$$\underline{\underline{\sigma}} = \left(K_o - \frac{2G}{3}\right)\varepsilon_v\,\underline{\underline{1}} + 2G\,\underline{\underline{\varepsilon}} - b\,p_p\,\underline{\underline{1}} \tag{2}$$

$$\frac{m^{fl}}{\rho_o^{fl}} = b\varepsilon_v + \frac{p_p}{M} \tag{3}$$

Biot's coefficient b and Biot's modulus M are defined by:

$$b = 1 - \frac{K_o}{K_s} \tag{4}$$

$$\frac{1}{M} = \frac{b-\phi_o}{K_s} + \frac{\phi_o}{K_{fl}} \tag{5}$$

where K_{fl} is the fluid bulk modulus.

Nonlinear elastic behavior is handled by deriving linear incremental stress-strain relations and introducing tangent elastic properties depending on the actual state.

Rock properties are usually studied through triaxial tests. The stress state in the rock sample is then axisymmetric and defined by the applied axial stress, confining pressure and pore pressure *(Fig. 1)*. The results are usually studied in terms of Terzaghi's effective mean pressure p' and deviatoric stress q, to which correspond the volumetric strain ε_v and the deviatoric strain ε_d:

$$p' = \frac{|\sigma_a| + 2p_c}{3} - p_p \qquad \varepsilon_v = \varepsilon_a + 2\varepsilon_r$$

$$q = |\sigma_a| - p_c \qquad \varepsilon_d = \frac{2}{3}|\varepsilon_a - \varepsilon_r|$$

This paragraph proposes a cemented structure model allowing the poroelastic properties of a rock to be estimated from its porosity and mineralogical content. This model is then applied to limestones and sandstones. In the case of sandstones, an additional effect of the stress state is taken into account.

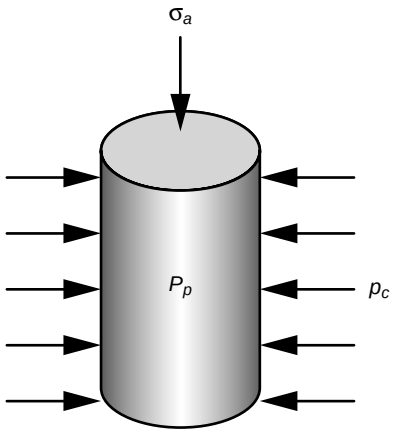

Figure 1

Stress and pressure state during a triaxial test.

1.1 Cemented Structure Model

Deriving the elastic properties of a compound material from the properties of its components is a very tempting approach. This goal can be achieved through different methods, among which the variational methods initiated by Hashin and Shtrikman (Watt *et al.*, 1976) and the theory of homogenization (Sanchez-Palencia, 1980). The theory of homogenization provides the right theoretical background, but its effective application requires powerful numerical tools (Poutet *et al.*, 1996), which do not conform to our specifications.

Hashin and Shtrikman have defined analytical upper and lower bounds for the bulk and shear moduli of an *n*-phase composite. These bounds correspond to the exact moduli of two model materials defined by an assemblage of identical composite spheres with no overlap. The composite spheres leading to the upper bound consist of a spherical particle of phase 1 and a set of concentric spherical shells of phases 2 to *n* (phases 1 to *n* being classified by increasing rigidity K_i), while the composite spheres leading to the lower bound are in reverse order *(Fig. 2)*. Both assemblages comply with the volume fraction of each phase. Direct application of this methodology to a porous rock is prevented by the zero "mechanical properties" of the pores, which systematically lead to zero lower bounds.

To overcome this difficulty, we adopt a two-level model (Vincké and Boutéca, 1992). The matrix elastic properties are first estimated using Hashin and Shtrikman's bounds:

$$K_s^- = K_1 + \frac{A_1}{1+\alpha_1 A_1} \quad \text{and} \quad K_s^+ = K_n + \frac{A_n}{1+\alpha_n A_n} \tag{6a, b}$$

$$G_s^- = G_1 + \frac{1}{2}\frac{B_1}{1+\beta_1 B_1} \quad \text{and} \quad G_s^+ = G_n + \frac{1}{2}\frac{B_n}{1+\beta_n B_n} \tag{7a, b}$$

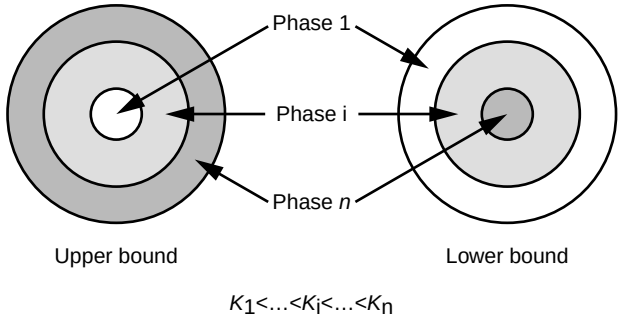

Figure 2

Composite spheres leading to Hashin and Strickman bounds.

where:

$$\alpha_1 = \frac{-3}{3K_1 + 4G_1} \qquad \alpha_n = \frac{-3}{3K_n + 4G_n}$$

$$A_1 = \sum_{i=2}^{n} \frac{f_i}{(K_i - K_1)^{-1} - \alpha_1} \qquad A_n = \sum_{i=1}^{n-1} \frac{f_i}{(K_n - K_i)^{-1} - \alpha_n}$$

$$\beta_1 = -\frac{3(K_1 + 2G_1)}{5G_1(3K_1 + 4G_1)} \qquad \beta_n = -\frac{3(K_n + 2G_n)}{5G_n(3K_n + 4G_n)}$$

$$B_1 = \sum_{i=2}^{n} \frac{f_i}{[2(G_i - G_1)]^{-1} - \beta_1} \qquad B_n = \sum_{i=1}^{n-1} \frac{f_i}{[2(G_n - G_i)]^{-1} - \beta_n}$$

The volume fraction of each mineral f_i is calculated with respect to the matrix volume and not the bulk volume, which includes the pore volume.

The dry rock is still viewed as the combination of a solid matrix occupying a volume fraction $(1-\phi)$ and a porous space occupying a volume fraction ϕ. The elastic moduli K_s and G_s of the solid matrix are taken equal to the upper or lower bounds defined by Equations (6) and (7), or to their mean value. The originality of the model is to consider that the pores contain cement of elastic moduli K_c and G_c, supposed to be submitted to the same stresses as the solid matrix and to deform in the same manner as the porous space.

Take an elementary representative volume of this cemented structure submitted to an isotropic stress $\underline{\underline{\sigma}} = -p\underline{\underline{1}}$ and no pore pressure. This loading yields the volumetric strain:

$$\varepsilon_v = -\frac{p}{K_o} \tag{8}$$

The stress partition theorem $\underline{\underline{\sigma}} = (1-\phi)\underline{\underline{\sigma}}^s - \phi\, p_p \underline{\underline{1}}$ (Coussy, 2004) leads to a stress in the solid matrix and an induced volumetric strain given by:

$$\underline{\underline{\sigma}}^s = -\frac{p}{1-\phi}\underline{\underline{1}}$$

$$\varepsilon_v^s = -\frac{p}{(1-\phi)K_s} \tag{9}$$

The stress in the cement is by assumption equal to the stress in the solid matrix, which yields:

$$\underline{\underline{\sigma}}^c = \underline{\underline{\sigma}}^s = -\frac{p}{1-\phi}\underline{\underline{1}}$$

$$\varepsilon_v^c = -\frac{p}{(1-\phi)K_c} \tag{10}$$

Since the cement is supposed to follow the porous space deformation, its volumetric strain matches the pore volume variation:

$$\varepsilon_v^c = \frac{V_p - V_p^o}{V_p^o}$$

We then get the following strain partition:

$$\varepsilon_v = \frac{V_b - V_b^o}{V_b^o} = \frac{V_s - V_s^o}{V_b^o} + \frac{V_p - V_p^o}{V_b^o} = (1-\phi_o)\varepsilon_v^s + \phi_o\,\varepsilon_v^c \tag{11}$$

Introducing Equations (8) to (10) into Equation (11) yields:

$$\frac{1}{K_o} = \frac{1-\phi_o}{1-\phi}\frac{1}{K_s} + \frac{\phi_o}{1-\phi}\frac{1}{K_c}$$

At order zero, the drained bulk modulus can finally be written as:

$$K_o = \frac{(1-\phi_o)K_s}{1-\phi_o + \phi_o\dfrac{K_s}{K_c}} \tag{12}$$

Combining Equations (4) and (12), we obtain a similar expression for Biot's coefficient:

$$b = \frac{\phi_o}{\phi_o + (1-\phi_o)\dfrac{K_c}{K_s}} \tag{13}$$

Take the same elementary representative volume and submit it to a uniaxial compressive stress along principal axis 1: $\underline{\underline{\sigma}} = -q\,\underline{e_1} \otimes \underline{e_1}$, with an induced deviatoric strain:

$$\varepsilon_d = \frac{2}{3}(\varepsilon_2 - \varepsilon_1) = \frac{q}{3G} \qquad (\varepsilon_2 = \varepsilon_3)$$

The stresses in the solid matrix and the cement are given by:

$$\underline{\underline{\sigma}}^s = \underline{\underline{\sigma}}^c = -\frac{q}{1-\phi}\,\underline{e_1} \otimes \underline{e_1}$$

and lead to the deviatoric strains:

$$\varepsilon_d^s = \frac{q}{(1-\phi)3G_s} \qquad \varepsilon_d^c = \frac{q}{(1-\phi)3G_c}$$

Assuming a strain partition according to the volume fractions occupied by the solid matrix and the porous space:

$\varepsilon_d = (1-\phi_o)\,\varepsilon_d^s + \phi_o\,\varepsilon_d^c$, we finally obtain the following expression for the shear modulus at order zero:

$$G = \frac{(1-\phi_o)\,G_s}{1-\phi_o+\phi_o\,\dfrac{G_s}{G_c}} \tag{14}$$

The remaining poroelastic parameter, Biot's modulus M, can be simply inferred from Equations (5) and (13). In many cases, the term $(b-\phi_o)/K_s$ is negligible and M can be directly estimated knowing the porosity and the fluid compressibility:

$$M \cong \frac{K_{fl}}{\phi_o} \tag{15}$$

1.2 Application to Limestones

Limestones are mainly made of calcite and usually show a linear behavior in the elastic domain. Their elastic properties can then theoretically be considered as independent of the stress state and obtained by taking calcite characteristics for the solid matrix.

We dispose of experimental data regarding limestones of porosities ranging from 4 to 45%, both from tests conducted at *IFP* and from the literature. The available properties are essentially values of the drained bulk modulus and Biot's coefficient measured under an isotropic loading. But, some measures of the shear modulus have also been made under a triaxial loading (defined by an axial or vertical stress and a confining pressure, which determines two equal horizontal stresses).

According to Equation (13), Biot's coefficient depends on only two parameters: the porosity and the ratio of the cement and solid matrix bulk moduli. Values of K_c/K_s can then be directly deduced from data on Biot's coefficient alone. Experimental data obtained at *IFP* on five different limestones (Larrys, Tavel, Vilhonneur, Lavoux and Estaillades) show no specific trend of this ratio as a function of porosity *(Fig. 3)*. K_c/K_s is thus taken as a constant common to every limestone. *IFP* data lead to a fitting value of 0.07 with an associated maximum error of ± 0.02. These data are plotted in Figure 4 together with independent data taken from Charlez and Heugas (1992), Gourri (1991) and Engstrøm (1992). The complete set of experimental results appear to follow reasonably well the curve predicted by Equation (13). However, for chalks the model seems to underestimate Biot's coefficient.

The experimental data on Larrys, Tavel, Vilhonneur, Lavoux and Estaillades limestones also comprise values of Biot's modulus. These measurements are coherent with the approximation given by Equation (15) (Boutéca *et al.*, 1991).

Taking K_c/K_s and assuming that the solid matrix bulk modulus is close to the bulk modulus of the calcite: K_s = 72.6 MPa, Equation (12) allows the drained bulk modulus of limestones to be estimated as a function of porosity. Figure 5 compares the corresponding predicted curve to various experimental data obtained at *IFP* or taken from Charlez and Heugas (1992) and Gourri (1991). Again, the model is consistent with the experimental trend.

To estimate the shear modulus from Equation (14) requires the knowledge of the solid matrix shear modulus and the ratio of the cement and solid matrix shear moduli. In coherence with the approach adopted for the estimation of the bulk modulus, we make the two following assumptions: the solid matrix shear modulus is close to the shear modulus of calcite: G_s = 31.6 MPa and G_c/G_s is a constant common to every limestone. *IFP* data on three different limestones

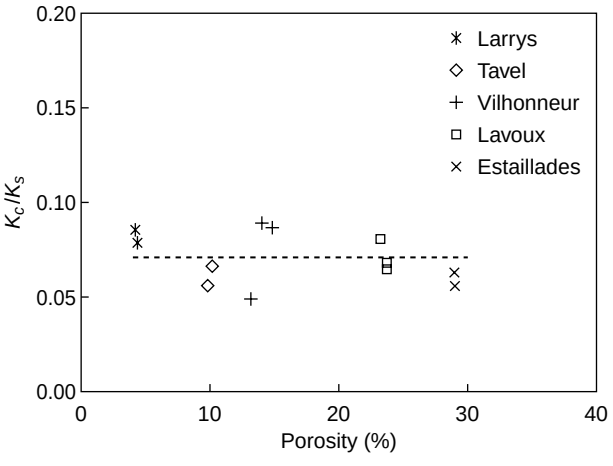

Figure 3

Ratio of limestone cement and solid matrix bulk moduli. *IFP* experimental data.

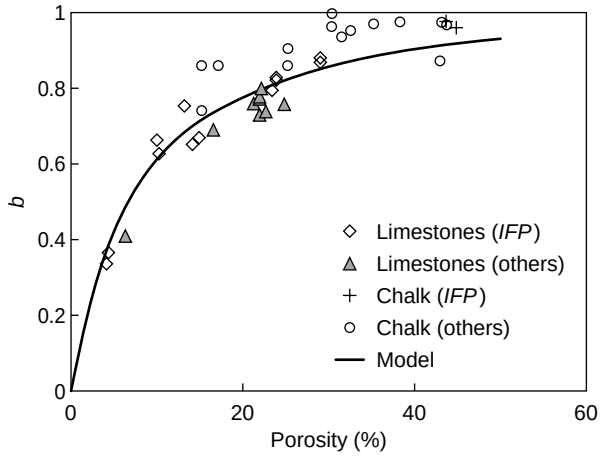

Figure 4

Prediction of Biot's coefficient of limestones as a function of porosity.

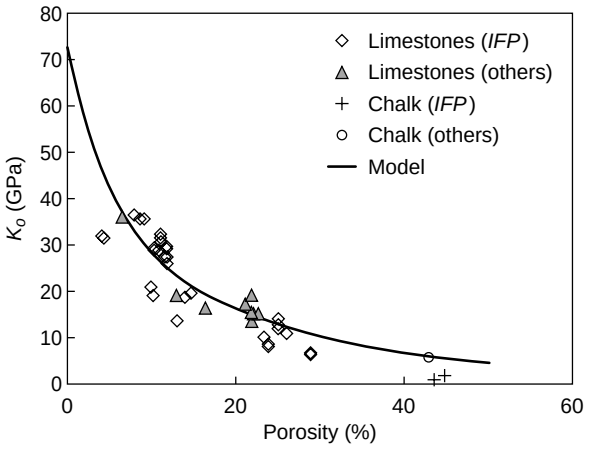

Figure 5

Prediction of the drained bulk modulus of limestones as a function of porosity.

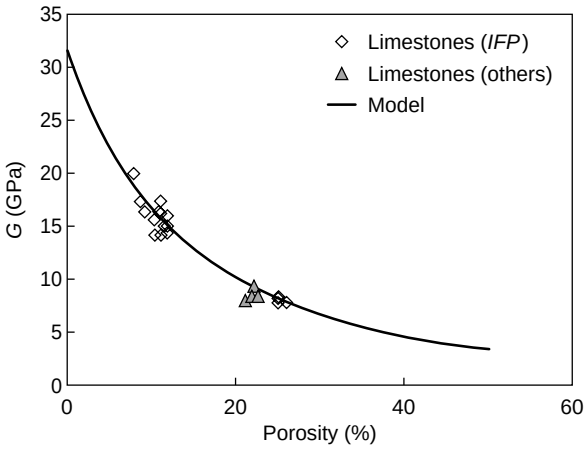

Figure 6

Prediction of the shear modulus of limestones as a function of porosity.

(Tavel, Vilhonneur and Lavoux) give $G_c/G_s = 0.12$. These data are plotted in Figure 6 together with independent data taken from Charlez and Heugas (1992). Further data would be needed to fully confirm Equation (14), but the available data already shows the global consistency of the model.

The collected data allow one to conclude that a reasonable estimation of elastic parameters of limestones can be obtained from Equations (12-15) with:

$$K_s = 72.6 \text{ MPa} \quad \text{and} \quad K_c/K_s = 0.07$$

$$G_s = 31.6 \text{ MPa} \quad \text{and} \quad G_c/G_s = 0.12$$

which yields the following elastic moduli for the cement:

$$K_c = 5.1 \text{ MPa} \quad \text{and} \quad G_c = 3.8 \text{ MPa}$$

1.3 Application to Sandstones

Sandstones are much more difficult to address. First, their composition is very variable. Second, their elastic properties depend on the stress state due to their often nonlinear behavior. Moreover, complete sets of experimental data, providing both elastic properties and whole mineral content, are rare.

An extensive experimental study has been conducted at the *Massachusetts Institute of Technology* on a large set of sandstones with porosities ranging from 5.2 to 30.5% (Caruso *et al.*, 1985; Wissler and Simmons, 1985; Wilkens *et al.*, 1986). The dry samples were submitted to a cyclic isotropic loading at confining pressures up to 200 MPa. All tested samples exhibit a nonlinear elastic behavior. For each elastic reloading, the tangent elastic compressibility was determined as a function of the applied confining pressure. Four levels of confining pressure were studied: 10, 30, 50 and 100 MPa. Caution is advised concerning the data obtained at 100 MPa due to possible sample damage.

The mineral content of the sandstones studied is described through six mineral classes. Table 1 gives the bulk and shear moduli taken for each mineral class. We assume that the solid matrix bulk modulus is independent of the stress state, which amounts to considering a solid matrix with no microcracks. Using Hashin and Shtrikman's method, the mineral content and porosity data given in Table 2 allow one to determine upper and lower bounds for the solid matrix bulk modulus of each sample. Samples comprising a significant amount of clay show lower modulus values and a greater difference between the two bounds. Figure 7 gives the relative difference between the upper and lower bounds for the solid matrix bulk modulus as a function of the clay content (expressed as a percentage of the total volume).

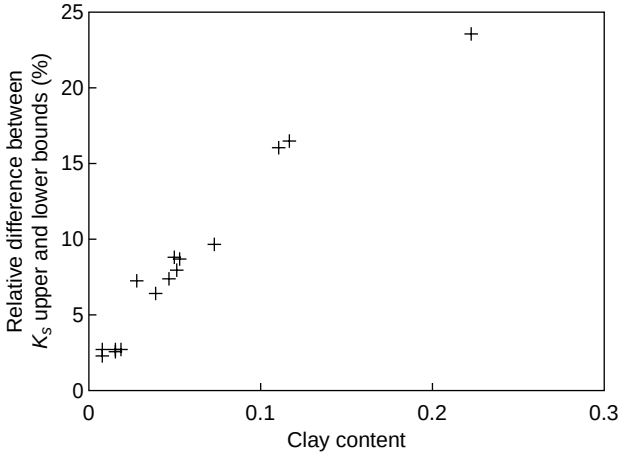

Figure 7

Effect of the clay content on the difference between Hashin and Shtrikman bounds for the solid matrix bulk modulus of sandstones.

TABLE 1

Mineral class moduli

Mineral class	***K* (GPa)**	***G* (GPa)**
Clay	6.75	4.925
Quartz	38	32
Muscovite	51.6	30
K-feldspar	53.6	27.1
Calcite	72.6	31.6
Dolomite	93.9	45.6

Knowing the solid matrix bulk modulus, K_c/K_s can be deduced from Equation (12) and the experimental drained bulk modulus. Hashin and Shtrikman's lower and upper-bounds lead to K_c/K_s values which are rather scattered and show no specific trend as a function of porosity *(Fig. 8)*. The increase of K_c/K_s with the confining pressure denotes sandstones nonlinear behavior. As for limestones, K_c/K_s is finally supposed to be common to every sandstone. A variation with the confining pressure is nevertheless allowed to take into account the nonlinear behavior. A theoretical study based on Biot's semilinear porelasticity has shown that the bulk modulus is effectively an increasing function of Terzaghi's effective mean pressure $(p - p_p)$ with no effect of the deviatoric stress (Bemer *et al.*, 2001).

Figure 9 shows a comparison of the predicted and measured values at the different confining pressure levels. Except for sample 2534, the theoretical and experimental bulk moduli lie within a range of ± 5 GPa.

The increase of K_c/K_s with the effective mean pressure can be represented by Hertz's contact model, which leads to a cement bulk modulus increasing as $(p - p_p)^{1/3}$ (Vincké, 1994). We then get the following expression for the

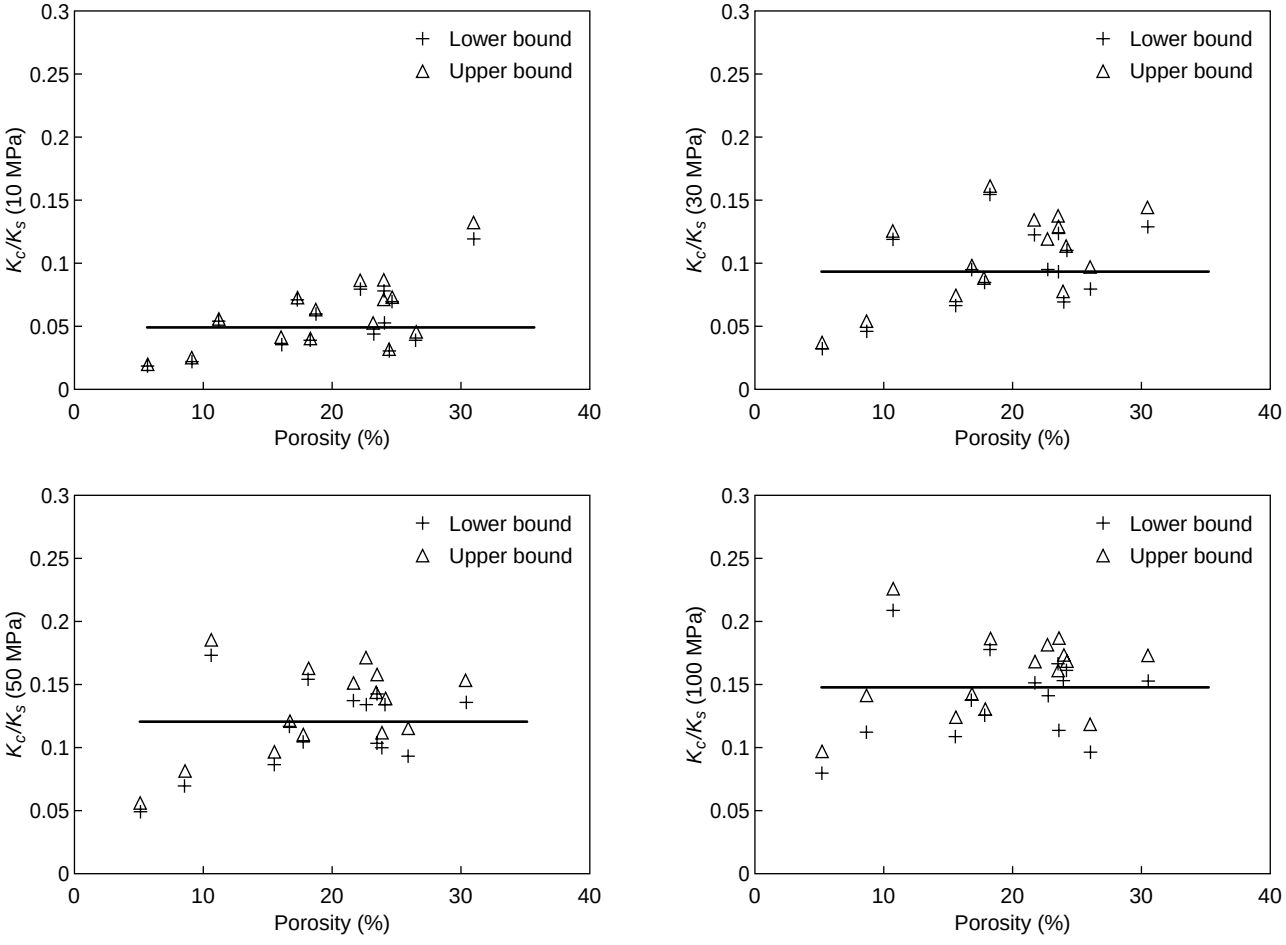

Figure 8

Ratio of sandstone cement and solid matrix bulk moduli at different confining pressure levels. Experimental data taken from Wissler and Simmons (1985).

TABLE 2

Porosity and mineral content of various sandstones (Caruso *et al.*, 1985)

Sample	Porosity	Clay	Quartz	Muscovite	K-feldspar	Calcite	Dolomite
2534	0.052	0.028	0.664	0	0.019	0.237	0
2694	0.085	0.073	0.842	0	0	0	0
2519	0.106	0.018	0.876	0	0	0	0
2093	0.156	0.051	0.675	0.042	0.076	0	0
2523	0.168	0.008	0.749	0	0.017	0.058	0
2124	0.178	0.008	0.781	0	0	0	0.033
2509	0.181	0.016	0.778	0	0.025	0	0
2513	0.217	0.039	0.744	0	0	0	0
2701	0.227	0.116	0.541	0	0.116	0	0
2700	0.234	0.046	0.689	0	0.031	0	0
2089	0.235	0.222	0.497	0.008	0.038	0	0
2704	0.238	0.053	0.648	0	0.061	0	0
2521	0.241	0.015	0.736	0	0.008	0	0
2698	0.259	0.111	0.556	0.007	0.067	0	0
2710	0.305	0.049	0.577	0	0.069	0	0

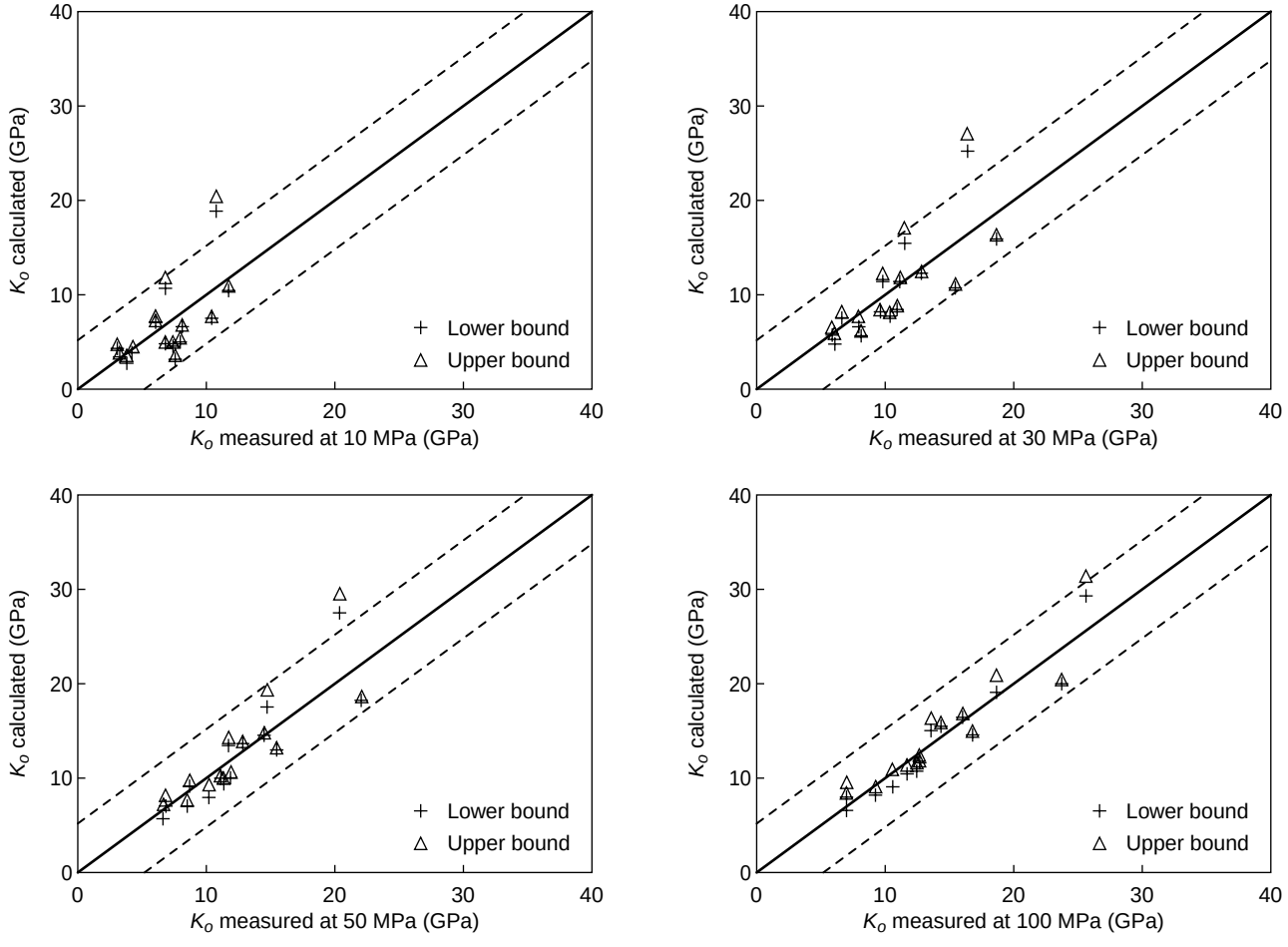

Figure 9

Comparison of predicted and measured drained bulk moduli of sandstones at different confining pressure levels. Experimental data taken from Wissler and Simmons (1985).

evolution of the tangent drained bulk modulus with Terzaghi's effective mean pressure:

$$K_o^t = \frac{(1-\phi_o)K_s}{1-\phi_o + \dfrac{\phi_o}{a\left(p-p_p\right)^{1/3}}} \tag{16}$$

The constant a is determined from the value of K_c/K_s corresponding to a 50 MPa confining pressure: $a = 0.33$. Figure 10 shows that Hertz's model represents reasonably well the experimental fitting values of K_c/K_s. Figure 11 illustrates the application of Equation (16) to the complete set of experimental data. The samples can be divided in two groups. Samples of group A verify the model and so validate the proposed approach.

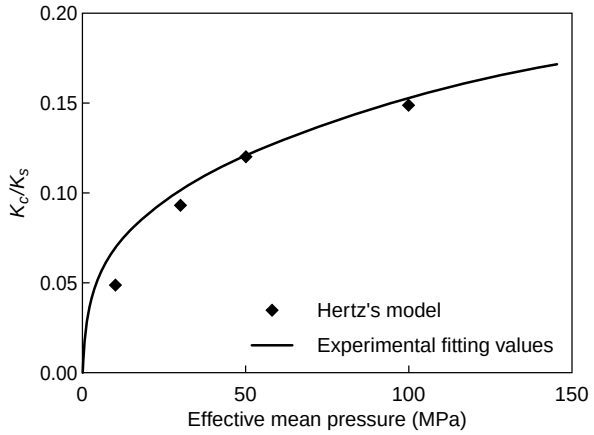

Figure 10

Evolution of K_c/K_s as a function of the effective mean pressure.

The bulk modulus of group B samples seems first to increase more or less linearly and/or present a stable value above some stress level. Vincké (1994) has shown that this behavior is representative of a microcracked rock and follows the model proposed by Walsh and Grosenbaugh (1979). To be applied, this model requires the knowledge of the microcracks closure pressure above which the bulk modulus remains constant. Since this value can not be deduced from log data and since group B predicted moduli are not aberrant, the model defined by Equation (16) still constitutes a valuable approach.

Equation (16) remains to be validated on independent data. We dispose of isotropic tests conducted on Fontainebleau sandstones of different porosities. This sandstone can be considered as composed of only quartz. We then take $K_s = 38$ MPa. The tests provide measurements of the drained bulk modulus and Biot's coefficient under a maximum effective confining pressure of 60 MPa. Combining Equations (4) and (16), we obtain an expression for the tangent Biot's coefficient as a function of Terzaghi's effective mean pressure:

$$b^t = \frac{\phi_o}{\phi_o + (1-\phi_o)\,a\left(p-p_p\right)^{1/3}} \tag{17}$$

Figure 12 shows that the values predicted by taking $p - p_p = 60$ MPa are coherent with the experimental data.

Further data will be needed to achieve the model validation, especially for the shear modulus. Unfortunately, we have no complete set of data providing porosity, mineral content and shear modulus measurements. The theoretical study based on Biot's semilinear porelasticity has shown that, in the restrictive case of an axisymmetric stress state, the tangent shear modulus increases with the deviatoric stress (Bemer *et al.,* 2001). A way of representing the evolution of sandstones tangent shear modulus with the stress state could then be to allow a variation of G_c/G_s with the deviatoric stress in Equation (14).

1.4 Conclusion

The structure model defined by Equations (12-14) gives interesting results for limestones and sandstones. In the case of sandstones, an effect of the stress state on the poroelastic properties needs to be considered. Extensions of Equations (12) and (13) for the drained bulk modulus and Biot's coefficient have been proposed and tested. Deviations have been observed, but the global results are in reasonable agreement with the experimental values. Additional data are required to derive an extension of Equation (14) for the shear modulus.

2 FAILURE PROPERTIES

A failure criterion defines a domain in the stress space outside of which the rock cannot withstand the load. At the microscopic level, failure is associated to the coalescence of inter- and intragranular microcracks. Provided that the permeability is sufficient to ensure a homogeneous pore pressure distribution, rock failure is governed by Terzaghi's effective stress: $\underline{\underline{\sigma}}' = \underline{\underline{\sigma}} + p_p \underline{\underline{1}}$. As an example, a triaxial test conducted at confining pressure p_c and pore pressure p_p will lead to the same axial stress at failure as a triaxial test conducted at confining pressure $p_c - \Delta$ and pore pressure $p_c + \Delta$ (Vincké *et al.*, 1998; Boutéca and Guéguen, 1999).

This paragraph first illustrates the behavior of a rock submitted to a compressive loading up to failure through triaxial test results (Wong *et al.*, 1997; Zhu and Wong, 1997; Yale and Crawford, 1998; Schutjens and de Ruig, 1996; Schutjens *et al.*, 1998; Brawn and Jahns, 1998). Rock failure strongly depends on:

- the rock nature (limestones, sandstones, shales);
- the initial porosity;
- the loading path followed;

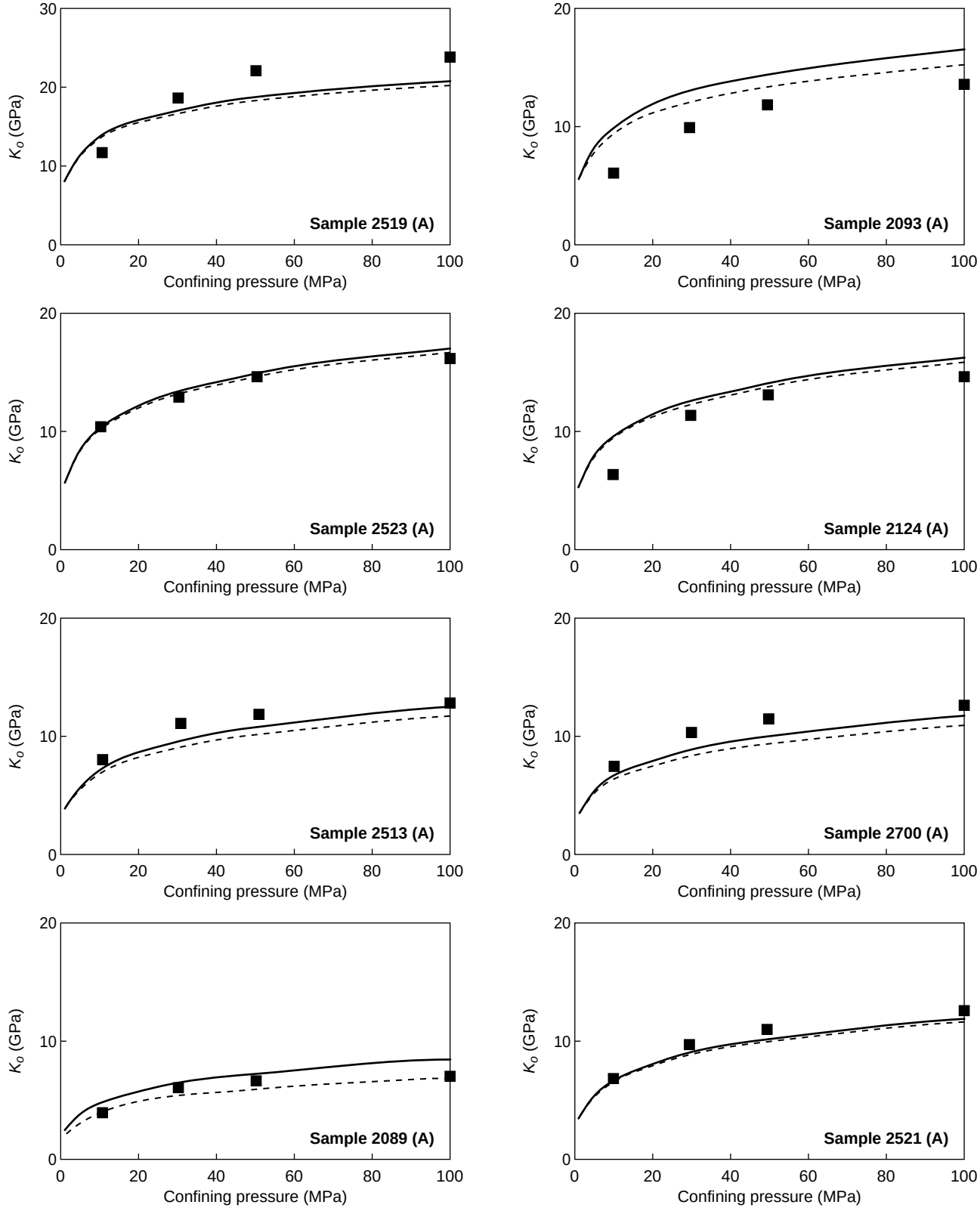

Figure 11

Predicted and measured tangent drained bulk moduli as a function of the confining pressure. Experimental data taken from Wissler and Simmons (1985).

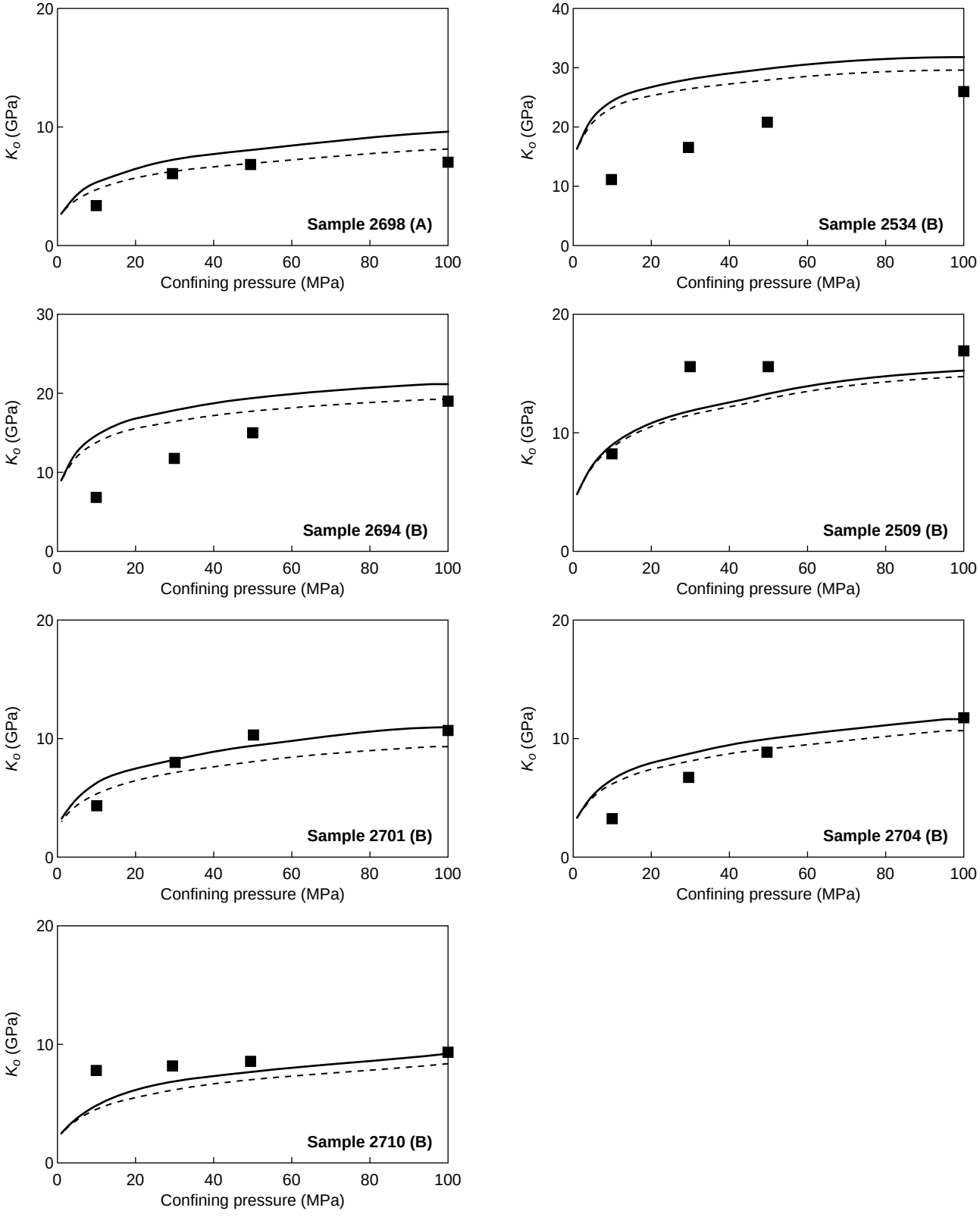

Figure 11

Predicted and measured tangent drained bulk moduli as a function of the confining pressure. Experimental data taken from Wissler and Simmons (1985).

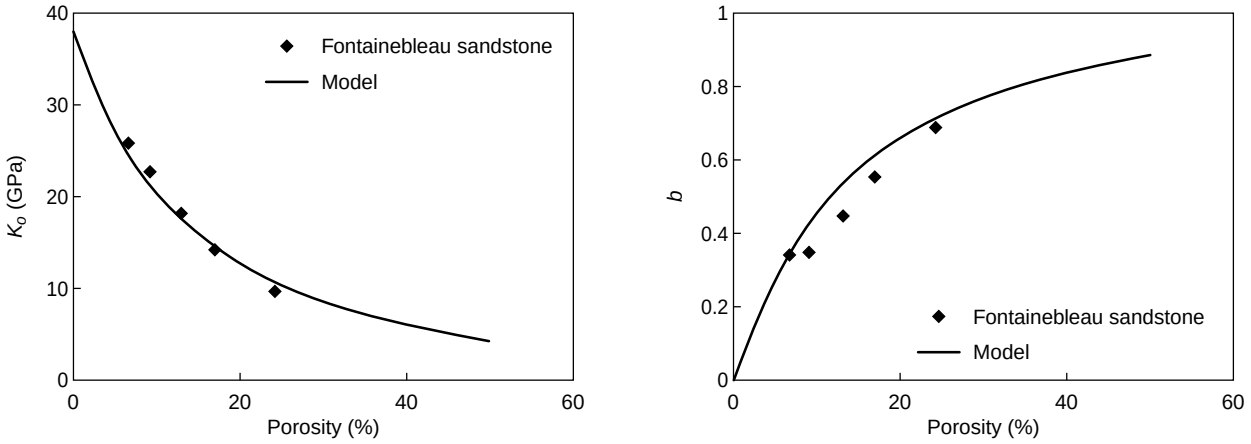

Figure 12

Prediction of the poroelastic properties of Fontainebleau sandstone measured at an effective confining pressure of 60 MPa.

and on various parameters such as the cementation and the grain size for sandstones (Wong *et al.*, 1997), the saturation state, especially for chalks (Homand and Shao, 2000a, 2000b; Matà, 2001), etc.

Specific failure criteria are then defined for limestones and sandstones. A distinction is made between cemented and poorly cemented sandstones. The proposed criteria require only the rock porosity as input data.

2.1 Behavior of a Rock Sample under a Compressive Loading

2.1.1 Sandstones

According to the loading path followed, the failure of a rock can be of two main types (Wong *et al.*, 1997; Zhu et Wong, 1997).

– Brittle failure occurs at low effective mean pressures. The sample fails by shear localization and a rapid decrease of its capacity to withstand a load is observed.

– At high effective mean pressures, the failure is induced by a compactive cataclastic flow corresponding to a homogeneously distributed microcracking. The rock being still able to carry a load under an increasing deformation, we use the term of ductile failure. Note that the deformation is then induced by sliding across many intercrossing shear planes and is thus not true plastic deformation.

A transitional type of failure, manifested by the development of several conjugate shear bands in the sample, is observed at intermediate effective mean pressures.

These failure modes are characterized by distinct critical stresses associated with different damage stages: micro-

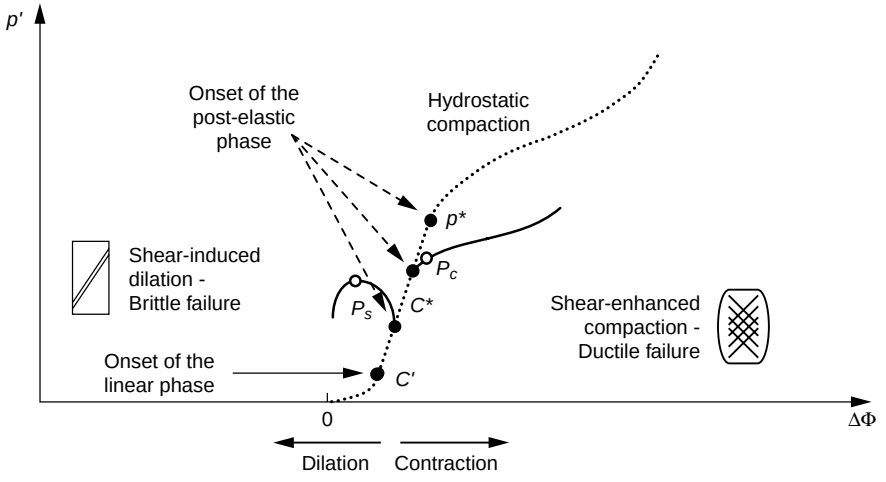

Figure 13

Response of a sandstone submitted to a compressive loading.

cracking, frictional slip, pore collapse, etc., which can notably be identified by measuring the acoustic emission activity.

Figure 13 represents the (Lagrangian) porosity evolution with the increase in effective mean pressure according to the loading path followed. The base of the curve corresponds to the closure of existing microcracks. The second part is linear and associated to the pore elastic deformation. The nonlinear third part happens after a critical effective pressure and depends on the loading path.

Hydrostatic (Isotropic) Loading

The curve $\Delta\Phi - p'$ presents a point of inflection at the critical effective pressure p^*, associated with the onset of grain crushing and pore collapse induced by the growth of transgranular microcracks.

Ductile Failure (Cataclastic Flow)

In comparison to the isotropic loading, the curve $\Delta\Phi - p'$ shows an additional porosity decrease induced by the deviatoric stress past an effective pressure C^* less than p^*. This phenomenon is referred to as shear-enhanced compaction. Beyond C^*, intragranular microcracks emanating from grain contacts start to expand, with a preferred orientation subparallel to the axial stress, whereas cracking in a sample hydrostatically loading beyond p^* is relatively isotropic. When they become transgranular, these microcracks induce a stress increase on the bearing grains and finally lead to grain crushing and pore collapse at the effective pressure P_c associated with a peak in the acoustic emission rate.

For consolidated sandstones, C^* and P_c values are very close and only C^* is used to characterize ductile failure.

Brittle Failure (Shear Localization)

In comparison to the isotropic loading, the curve $\Delta\Phi - p'$ shows a dilating behavior beyond an effective pressure C' far less than p^* and associated with damage onset. This phenomenon is referred to as shear-induced dilation. The deviatoric stress finally reaches a peak at an effective mean pressure P_s, which corresponds to the development of a shear band through the sample. Between C' and P_s, the acoustic emission activity is mainly due to intergranular cracking which allows relative movements of the grains inducing an overall dilation of the porous space. Intragranular cracks do not initiate until near the peak stress. The subsequent microcracks coalescence results in shear localization in the post-peak stage.

2.1.2 Limestones

Unlike sandstones, limestones may develop a significant "plastic" behavior before failure (Yale and Crawford, 1998). The term plastic only refers to a behavior showing irreversible strains without a decrease of the elastic properties. Plasticity is essentially encountered at high effective mean pressure and for rocks of high initial porosity, in particular for chalks.

Loading paths with low effective mean pressures lead to a brittle failure of the samples, while loading paths with high effective mean pressures allow two yield surfaces to be identified. The initial yielding surface at which the curve $\Delta\Phi - p'$ deviates from its linear slope by more than 10% is to be compared to the effective pressure C^* associated with the onset of shear-enhanced compaction in the case of sandstones. The hardening cap is reached at the point of inflection of the curve $\Delta\Phi - p'$ and thus corresponds to the effective pressure P_c associated with the onset of grain crushing and pore collapse in the case of sandstones.

The fundamental difference between limestones and sandstones lies in the significant gap between the two surfaces for limestones. As an example, the ratio between the effective mean pressures of hardening onset and initial yielding reaches 1.8 for 20% porosity limestones (Yale and Crawford, 1998). The porosity level mainly controls the sample yielding: the lower the porosity, the higher the effective mean pressure at initial yielding and the larger the gap between the hardening onset and the initial yielding.

In coherence with the case of sandstones, limestones ductile failure is supposed to occur when the hardening cap is reached.

2.2 Failure Criterion for Limestones

Brittle failure of limestones is commonly addressed by Coulomb's approach (Fjær *et al.*, 1992):

$$q = A + B\,p' \tag{18}$$

where parameters A and B are linked to the cohesion c' and the angle of internal friction φ':

$$A = \frac{6c'\cos\varphi'}{3-\sin\varphi'} \qquad B = \frac{6\sin\varphi'}{3-\sin\varphi'} \tag{19}$$

Data on c' and φ' for limestones can be found in the literature. But, actual stress values at failure are rare.

It remains to close the failure surface in the ductile domain. We adopt a circular cap surface as observed in chalks (Rhett and Teufel, 1992; Longuemare *et al.*, 1996):

$$q^2 + (p')^2 = (p^*)^2 \tag{20}$$

Figure 14 illustrates the resulting failure surface.

To ensure an easy handling of the model, we suppose that failure in limestones is mainly controlled by the rock porosity. Empirical correlations for the cohesion, the angle of internal friction and the grain crushing and pore collapse pressure are then derived from *IFP* data on Tavel, Vilhonneur and Lavoux limestones, and literature data (Rhett and Teufel,

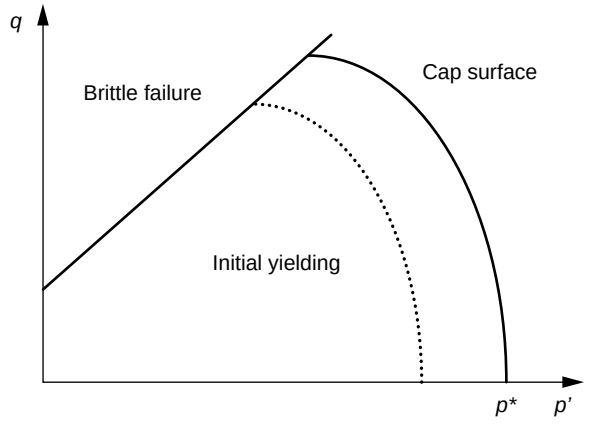

Figure 14

Failure criterion of a limestone.

1992; Gaviglio and Carrio, 1993). c' and p^* appear to follow exponential trends, while φ' trend is more or less linear.

$$c'(\phi) = c_o \exp[-\alpha_c \phi] \quad (21)$$

$$\varphi'(\phi) = \alpha_f \phi + \beta_f \quad (22)$$

$$p^*(\phi) = p_o \exp[-\alpha_p \phi] \quad (23)$$

with ϕ expressed in %, c_o = 40.3 MPa, α_c = 0.054, α_f = – 0.893°, β_f = 49.0°, p_o = 601.6 MPa and α_p = 0.083.

Figures 15, 16 and 17 show how those laws fit the experimental data. *IFP* experimental set-ups do not allow us to reach p^* for the 10 and 11% porosity limestones (Tavel and Vilhonneur). The actual experimental grain crushing and pore collapse pressures are then higher than the values denoted by "*IFP* min." (for minimum) in Figure 17.

Characterizing limestones failure with only one structural parameter naturally leads to rather scattered data. The point is now to verify that a coherent order of magnitude can be obtained from Equations (18-23). Figures 18 and 19 compare the predicted and experimental data for the three limestones tested at *IFP* and the North Sea chalks studied by Rhett and Teufel (1992). The model provides a reasonable fit to these specific experimental data, but further stress values at failure are needed to test its consistency on independent data.

2.3 Failure Criterion for Sandstones

Brittle failure points of sandstones show a distinct nonlinear trend which prevents use of Coulomb's failure criterion and thus definition of a cohesion and an angle of internal friction valid on an extended range of effective mean pressures. The ductile domain is closed by an elliptical cap surface. Figure 20 illustrates the resulting shape of the failure criterion. The transition from brittle to ductile failure is supposed to occur at a transitional effective mean pressure p_t.

Figure 21 shows stress values at failure for sandstones of porosities ranging from 14.5 to 35.5% (Wong *et al.*, 1997) *(Table 3)*. The failure points are rather scattered. However, the authors obtain a common envelope if the data are normalized by the grain crushing and pore collapse pressure. The same approach is followed by (Boutéca *et al.*, 2000).

When the loading deviates from a pure hydrostatic path, shear effects become significant and can not be fully addressed by a purely hydrostatic parameter. We thus choose to introduce a different normalizing pressure for the effective mean pressure and the deviatoric stress at failure. The effective mean pressure is still normalized by p^*, but the deviatoric stress is normalized by the product $m\,p^*$, where m is a dimensionless shear parameter.

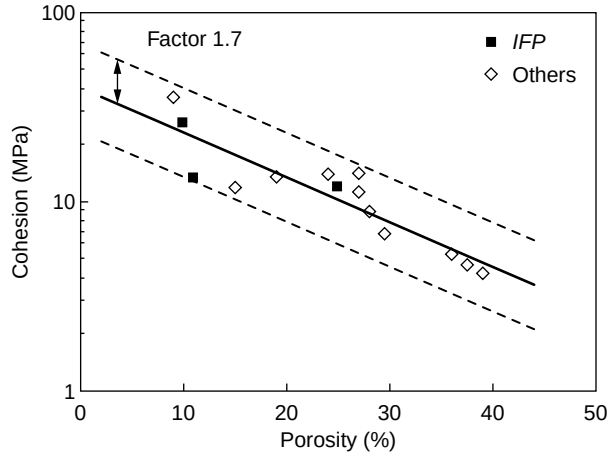

Figure 15

Empirical correlation between the cohesion and the porosity for limestones.

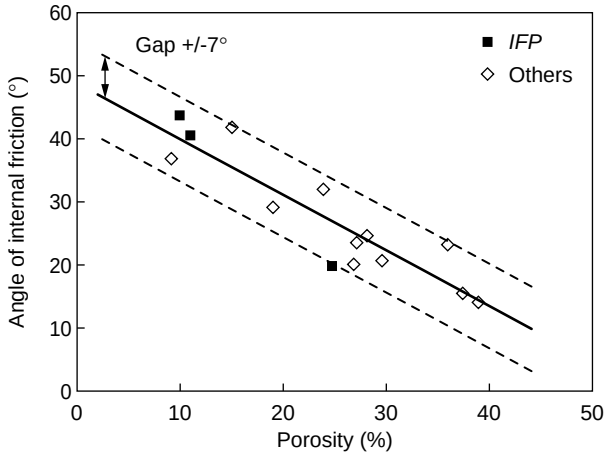

Figure 16

Empirical correlation between the angle of internal friction and the porosity for limestones.

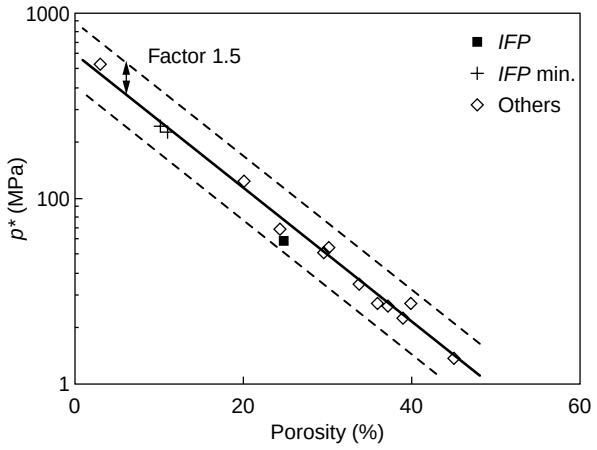

Figure 17

Empirical correlation between the grain crushing and pore collapse pressure and the porosity for limestones.

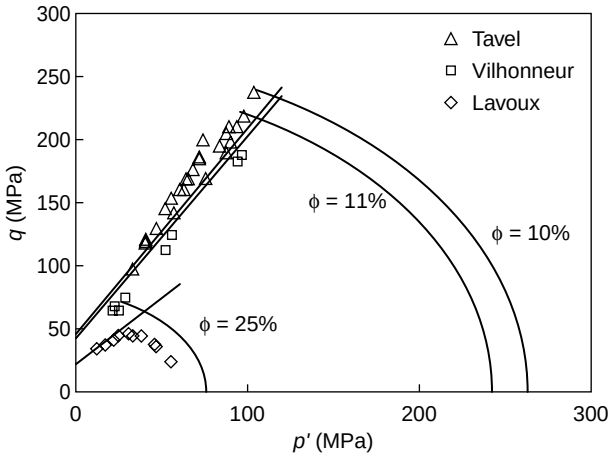

Figure 18

Prediction of *IFP* failure data for different limestones.

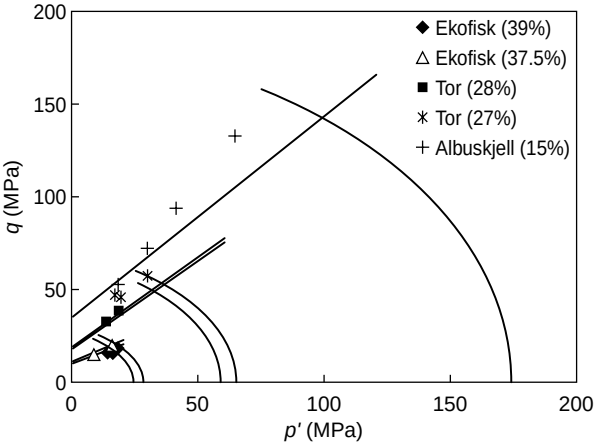

Figure 19

Prediction of failure data for North Sea chalks (Rhett and Teufel, 1992).

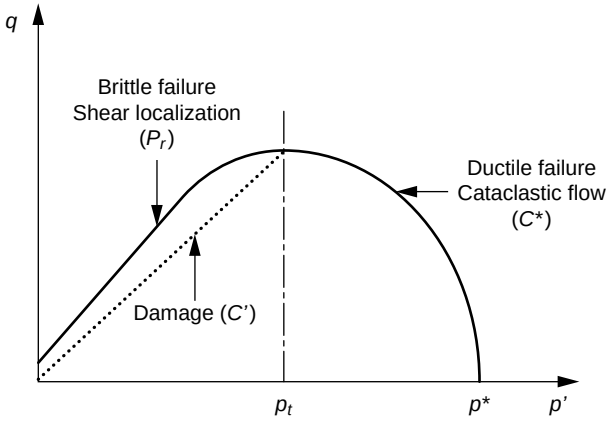

Figure 20

Failure criterion of a sandstone.

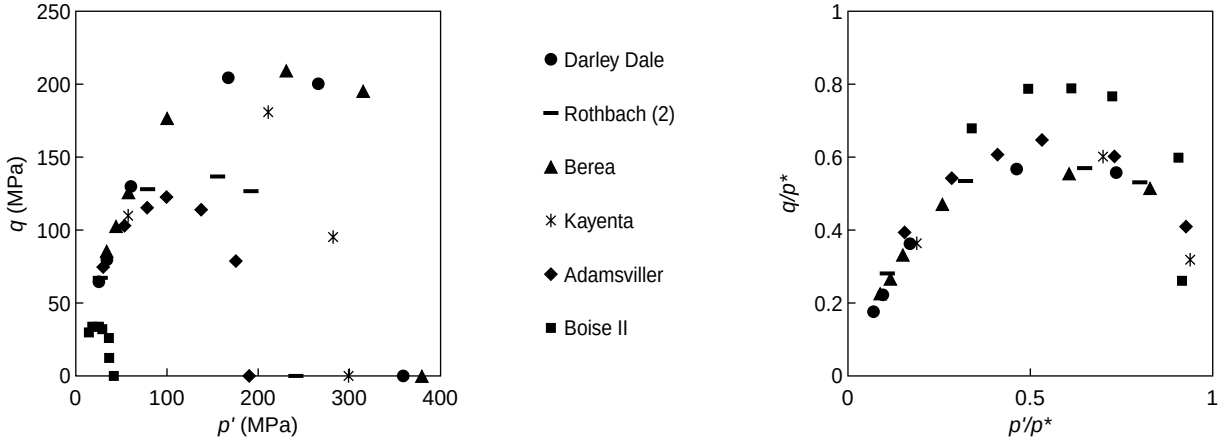

Figure 21

Experimental failure data for various sandstones (Wong *et al.*, 1997).

TABLE 3

Porosity and cementation level of various sandstones

Sandstone	Porosity (%)	Cementation	Paper
Darley Dale	14.5	cemented	(Wong *et al.*, 1997)
Rothbach (2)	19.9	cemented	(Wong *et al.*, 1997)
Berea	21	cemented	(Wong *et al.*, 1997)
Kayenta	21	cemented	(Wong *et al.*, 1997)
Adamsviller	22.6	cemented	(Wong *et al.*, 1997)
Boise II	35	cemented	(Wong *et al.*, 1997)
Wyoming	25	poorly cemented	(Zhang *et al.*, 1998)
Louisiana	25	poorly cemented	(Zhang *et al.*, 1998)
Saltwash	31	poorly cemented	(Zhang *et al.*, 1998)
North Sea	from 8.5 to 32.5	cemented	(Larsen *et al.*, 1998)
Tennessee	4.5-7.5	cemented	(Keaney *et al.*, 1998)
Sublette	4.3	cemented	(Lin, 1981)
Rio Blanco	21.8	cemented	(Lin, 1981)
Red Wildmoor	24	cemented	(Nicholson *et al.*, 1998)
Saltwash South	26-27.5	cemented	(Nicholson *et al.*, 1998)
Jurassic 3	34.5-37	poorly cemented	(Nicholson *et al.*, 1998)

The elliptical cap surface can then be expressed as:

$$\left(\frac{q}{m\,p^*}\right)^2 = \frac{p'}{p^*}\left(1-\frac{p'}{p^*}\right) \tag{24}$$

Knowing p^* (experimental value), ductile failure data allow m to be determined for each tested sandstone. Figure 22 shows the corresponding representation of Wong's ductile failure data, which leads to very limited scattering.

The brittle failure data are represented by a parabolic surface given by *(Fig. 23)*:

$$\frac{q}{m\,p^*} = a_s + b_s\frac{p'}{p^*} + c_s\left(\frac{p'}{p^*}\right)^2 \tag{25}$$

Knowing m and p^*, the values of a_s, b_s and c_s are fitted on Wong's brittle failure data. We derive: $a_s = 0.053$, $b_s = 1.563$ and $c_s = 1.392$ with a regression coefficient of 0.987, which indicates a good consistency of the failure criterion defined by Equation (25).

The damage criterion is taken as the straight line connecting the origin to the point of transition between brittle and ductile failure, which yields:

$$\frac{q}{p^*} = a_e\frac{p'}{p^*} \tag{26}$$

with $a_e = 0.805$. Figure 23 shows that this assumption is coherent.

Figure 24 shows that taking into account shear effects on failure via a different normalization of the effective mean pressure and the deviatoric stress actually leads to a better representation of the failure data than the equivalent normalization adopted by Wong *et al.* (1997) and Boutéca *et al.* (2000).

Complete failure data on three sandstones described as very friable can be found in Zhang *et al.* (1998) *(Table 3)*. The ductile failure data lead to m values lower than for cemented sandstones at a same porosity level. But, when normalized, the failure data of Zhang's poorly cemented sandstones appear to follow reasonably well the failure criterion defined for cemented sandstones *(Fig. 25)*. We thus keep the same normalized failure criterion for cemented and poorly cemented sandstones.

As in the case of limestones, we suppose that sandstone failure is mainly controlled by the rock porosity and search for empirical correlations for p^* and m. Figure 26 shows measures of p^* obtained on more or less cemented sandstones of various porosities. The whole set of data is coherent and leads to a common exponential correlation with a maximum factor of 2 between experimental and predicted data:

$$p^*(\phi) = p_o\exp\left[-\alpha_p\,\phi\right] \tag{27}$$

with $p_o = 3663.85$ MPa and $\alpha_p = 0.124$.

Figure 27 shows the two trends of the shear parameter for cemented and poorly cemented sandstones. For cemented sandstones, shear effects appear to intensify with the porosity, a higher porosity probably allowing more possible grains movements under shear. Poorly cemented sandstones seem less sensitive to shear effects.

Lacking additional data, we adopt a linear variation law for the cemented sandstones and a constant value equal to 1 for the poorly cemented sandstones:

$$m^c(\phi) = \alpha_m\,\phi + \beta_m \tag{28}$$

with $\alpha_m = 0.020$ and $\beta_m = 0.882$:

$$m^{pc} = 1 \tag{29}$$

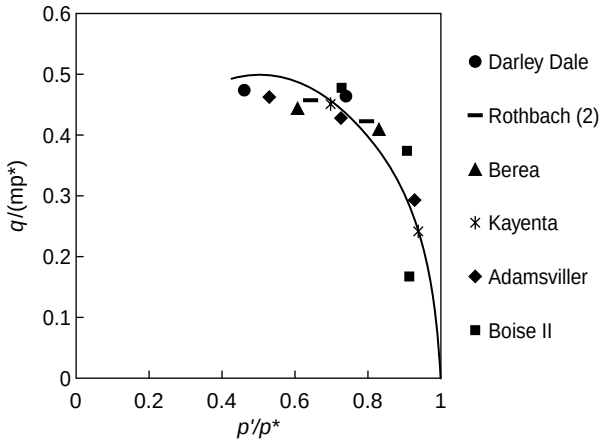

Figure 22

Normalized ductile failure criterion for sandstones. Experimental data from Wong *et al.* (1997).

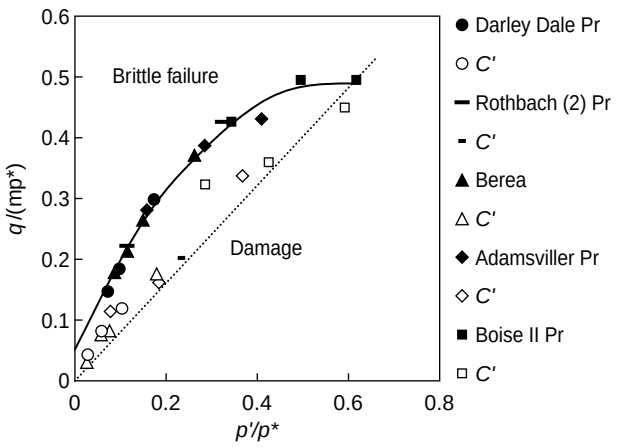

Figure 23

Normalized brittle failure criterion for sandstones. Experimental data from Wong *et al.* (1997).

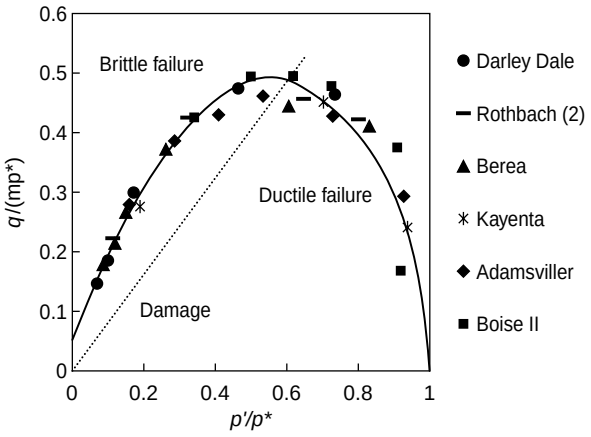

Figure 24

Global normalized failure criterion for sandstones. Cemented sandstones (Wong *et al.*, 1997).

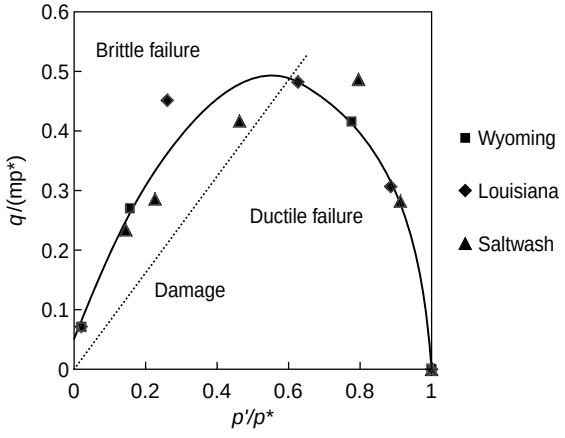

Figure 25

Global normalized failure criterion for sandstones. Poorly cemented sandstones (Zhang *et al.*, 1998).

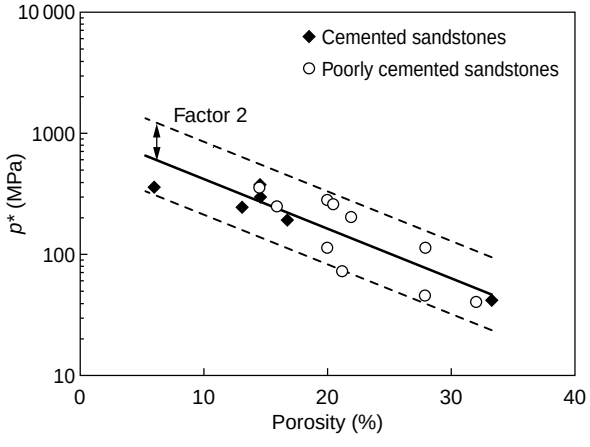

Figure 26

Empirical correlation between the grain crushing and pore collapse pressure and the porosity for sandstones.

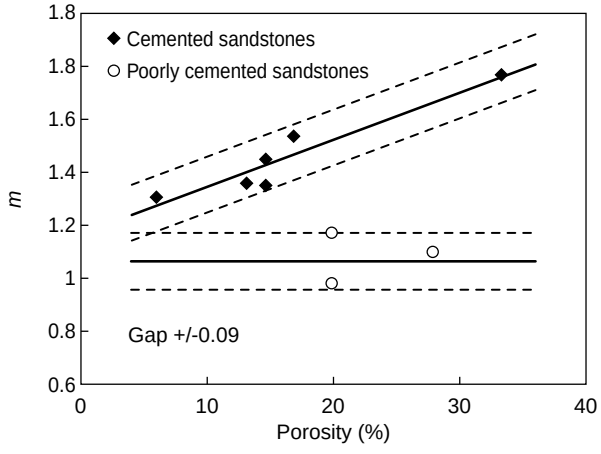

Figure 27

Empirical correlation between the shear parameter and the porosity for cemented and poorly cemented sandstones.

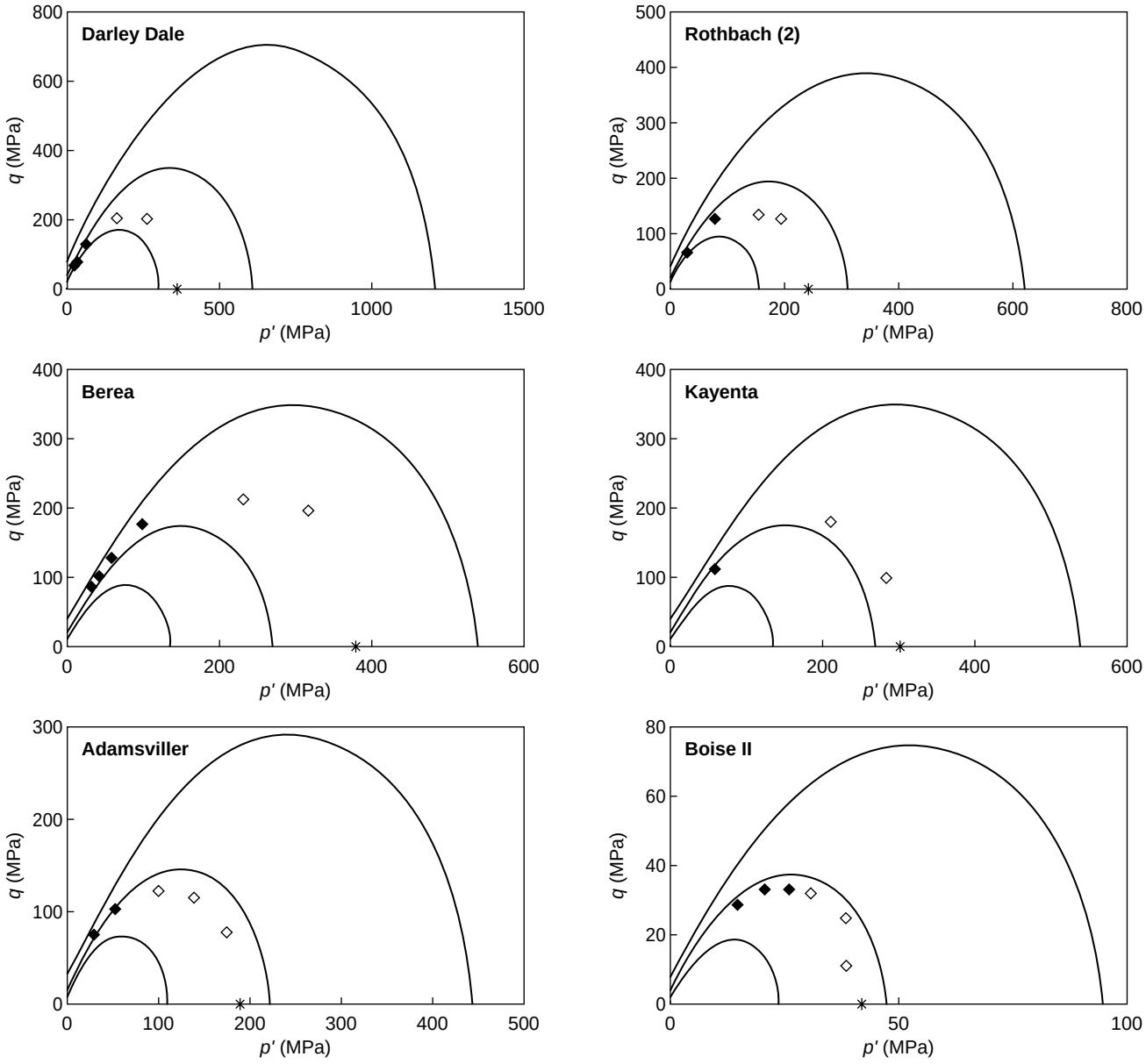

Figure 28

Prediction of the experimental data used to fit the failure model for cemented sandstones (black diamonds = brittle failure; white diamonds = ductile failure; star = grain crushing and pore collapse pressure).

Figures 28 and 29 show the prediction of Wong and Zhang's data from Equations (24) and (25). The value of m is directly deduced from Equations (28) or (29). Three values of p^* are however used to represent the incertitude associated with the estimate of the grain crushing and pore collapse pressure: the middle curve is obtained using Equation (27), while the upper and lower curves correspond to twice and half the predicted value. The failure model thus allows the experimental data to be bounded. Moreover, the largest differences compared to the actual predicted curve are obtained for ductile failure. Brittle failure, which is the failure mode generally encountered while drilling, is rather correctly represented *(Fig. 30)*.

The failure criterion defined by Equations (24, 25, 27 and 28 or 29), remains to be validated on independent data. Figure 31 compares experimental data normalized via Equations (27 and 28 or 29) to the theoretical failure criterion

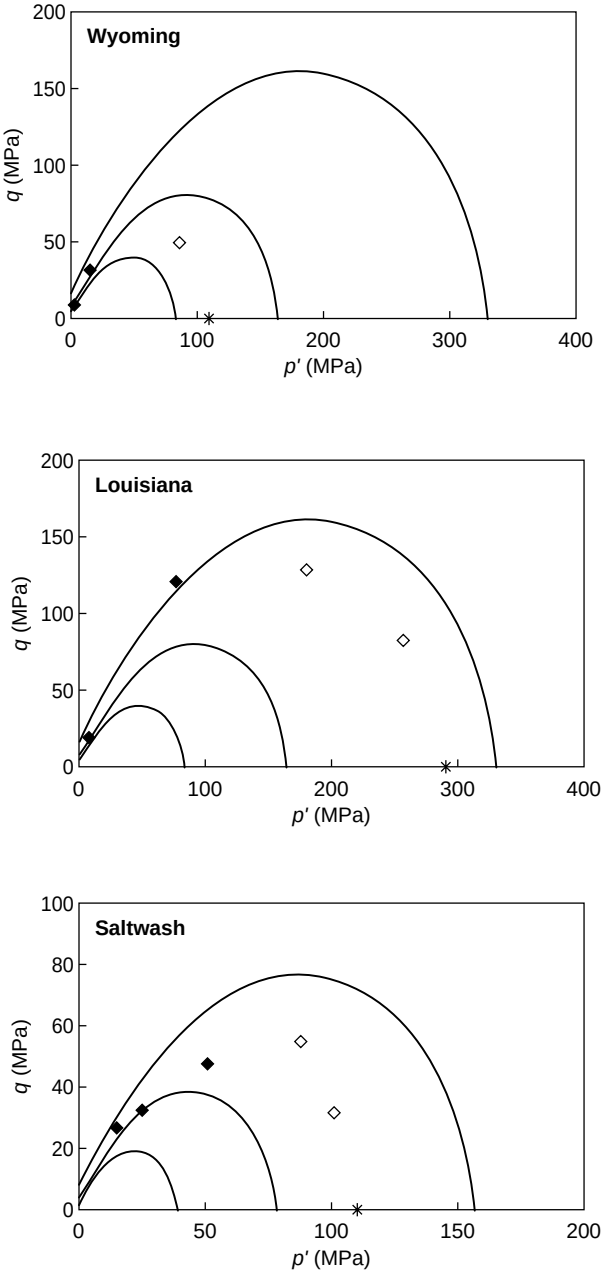

Figure 29

Prediction of the experimental data used to fit the failure model for poorly cemented sandstones (black diamonds = brittle failure; white diamonds = ductile failure; star = grain crushing and pore collapse pressure).

defined by Equations (24 and 25). These data cover a wide range of porosity *(Table 3)*, but mainly concern brittle failure and only one poorly cemented sandstone (Jurassic 3). The experimental data turn out to be rather close to the actual predicted curve and always fall within the upper and lower bounds defined by using twice and half the grain crushing and pore collapse pressure predicted by Equation (27).

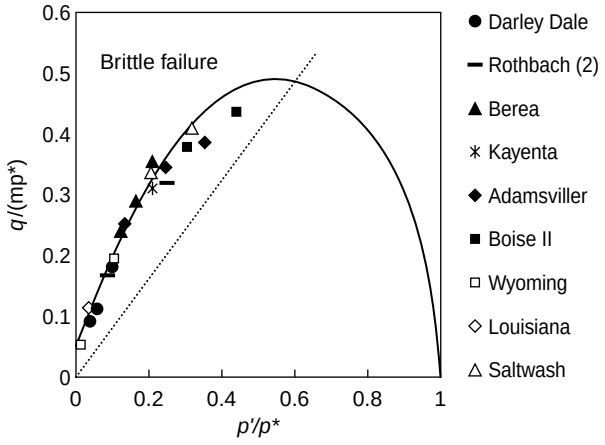

Figure 30

Prediction of brittle failure data in the domain $p'/p^* < 0.45$.

2.4 Conclusion

Two distinct failure criteria have been defined for limestones and sandstones. Both models require only the knowledge of the porosity and of the level of cementation for sandstones (cemented or poorly cemented). The failure criterion for limestones is linear for brittle failure and represents ductile failure by a circular cap surface. In the case of sandstones, a normalized failure criterion has been defined leading to a parabolic brittle failure surface and an elliptical cap surface for ductile failure. Correlations between the normalization parameters and the porosity have been proposed.

The failure criteria thus defined have been tested on various experimental data. The results obtained show that they provide reasonable estimations of the stresses at failure. Additional data will help to specify the associated errors.

3 DEDICATED SOFTWARE

Dedicated software has been developed for the Windows environment. This tool integrates the models proposed in this paper and aims at estimating rock mechanical properties and comparing the results to experimental data. It has been designed to allow every engineer to easily use the models. The software is divided into three parts *(Fig. 32)*. Part 1 reads in the set of input data for the selected model and calculates the associated mechanical properties. Part 2 ensures the storage of experimental data. Part 3 runs the graphic display of the results; in particular visual comparisons between computed and experimental data can be made.

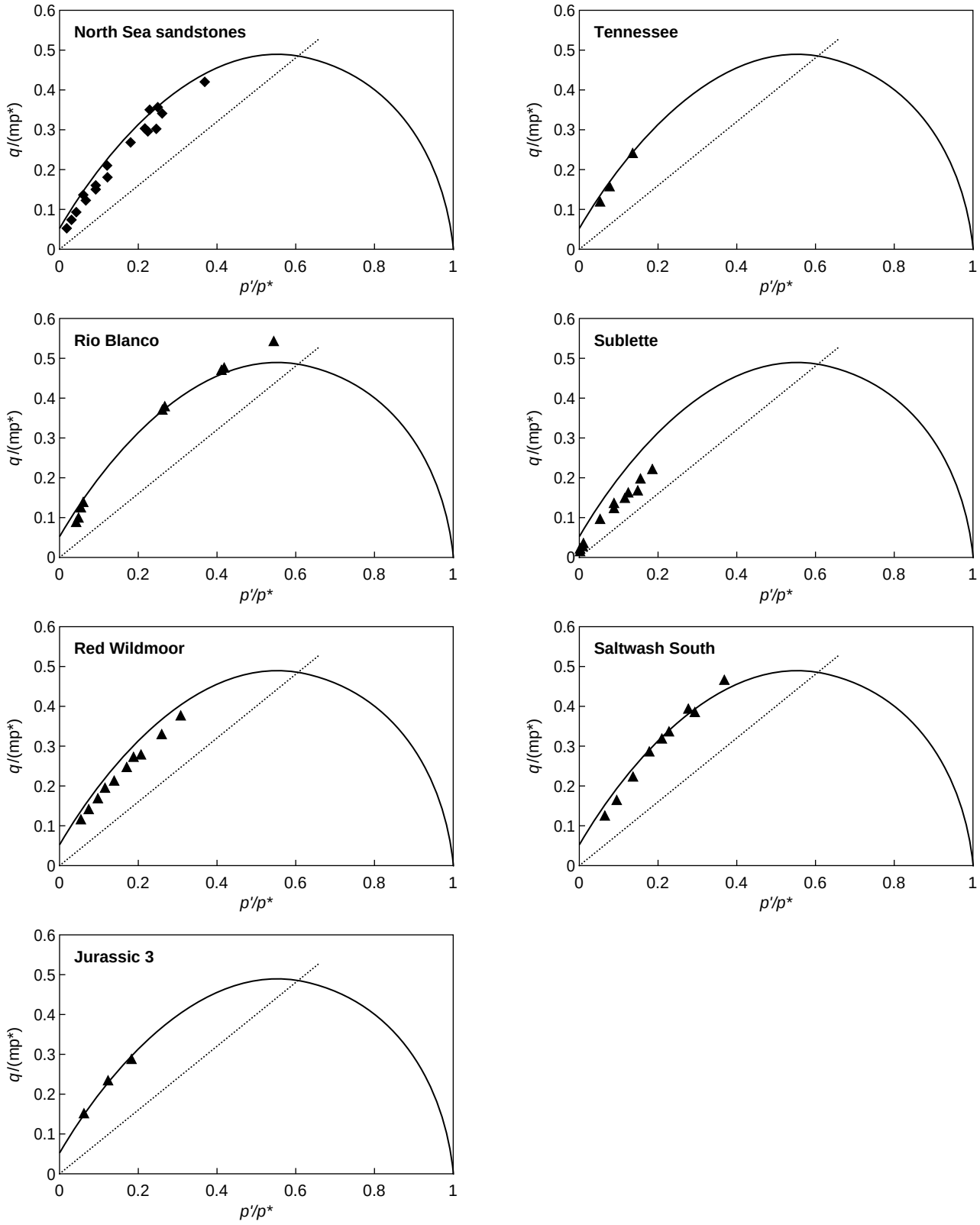

Figure 31

Prediction of the stresses at failure for various sandstones.

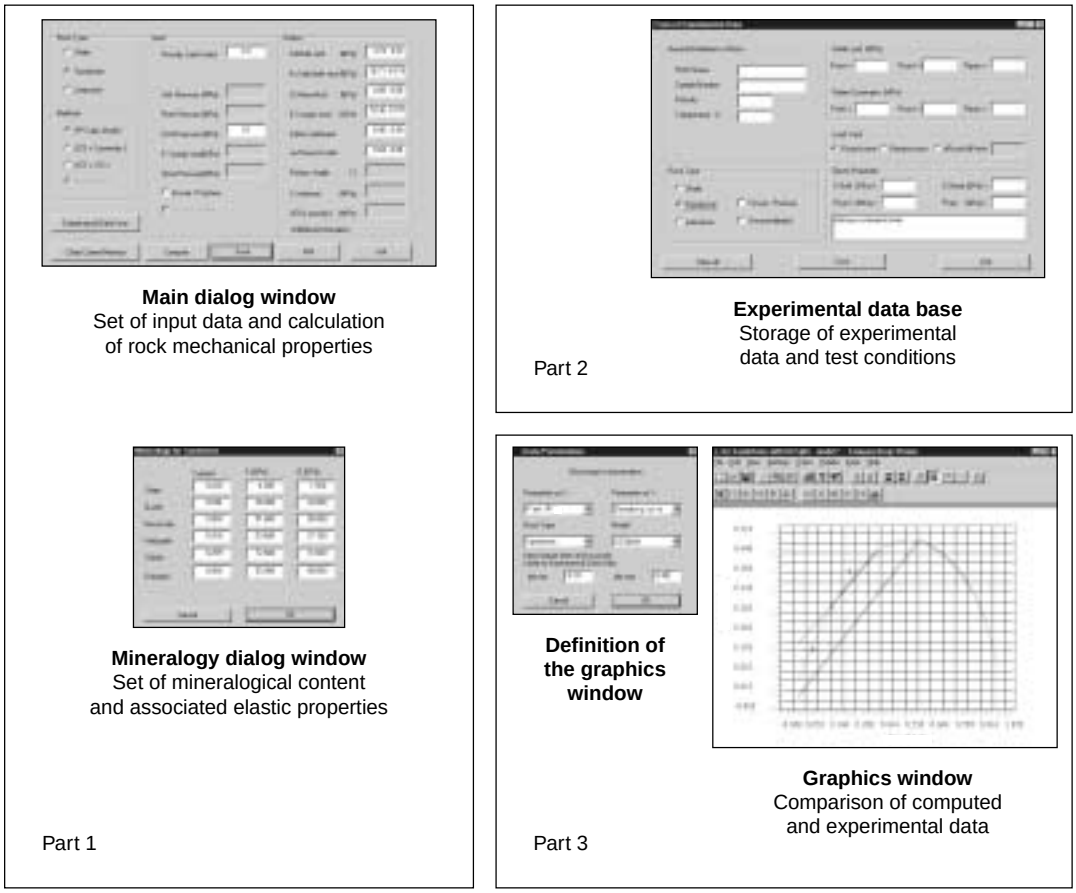

Figure 32

General structure of the software.

GENERAL CONCLUSION

In this paper, we propose analytical models allowing one to estimate poroelastic and failure properties of limestones and sandstones directly from their porosity and, in the specific case of poroelastic characteristics of sandstones, their mineral content. The properties obtained are in reasonable agreement with experimental data. Further data are nonetheless required to specify the evolution of the shear modulus of sandstones as a function of the stress state and to characterize the errors associated with the various models.

Dedicated software has been developed to easily compute rock mechanical properties from the models defined and compare the calculated values to stored experimental data.

The second step of the project will be to infer the input data for the models (porosity and mineral content) from drilling logs and compare the obtained results to tests on core samples. A geomechanical log could then be automatically created from standard logs and help to optimize drilling. We also intend to check the suitability of this approach for plastic properties and shales behavior.

REFERENCES

Bemer, E., Boutéca, M., Vincké, O., Hoteit, N. and Ozanam, O. (2001) Poromechanics: From Linear to Nonlinear Poroelasticity and Poroviscoelasticity. *Oil & Gas Science and Technology - Revue de l'IFP*, **56**, 6, 531-544.

Biot, M.A. (1973) Nonlinear and Semilinear Rheology of Porous Solids. *J. Geoph. Res.*, **78**, 23, 4924-4937.

Boutéca, M., Sarda, J.P. and Laurent, J. (1991) Rock Mechanics Contribution to the Determination of Fluid Flow Properties. SCA - Advances in Core Evaluation II - Reservoir appraisal. *2nd European Symposium of the Society of Core Analysts*, May 20-22 1991, London. Gordon and Breach Science Publishers, Philadelphia.

Boutéca, M. and Guéguen, Y. (1999) Mechanical Properties of Rocks: Pore Pressure and Scale Effects. *Oil & Gas Science and Technology – Revue de l'IFP*, **54**, 6, 703-714.

Boutéca, M.J., Sarda, J.P. and Vincké, O. (2000) Constitutive Law for Permeability Evolution of Sandstones During Depletion. *Paper SPE 58717.*

Brawn, R. and Jahns, E. (1998) Cracking and Compaction Behavior of Sandstone. *Paper SPE/ISRM 47377.*

Caruso, L., Simmons, G. and Wilkens, R. (1985) The Physical Properties of a Set of Sandstones - Part I. The Samples. *Int. J. Rock. Mech. Min. Sci. & Geomech. Abstr.*, **22**, 6, 381-392.

Charlez, Ph.A. (1991) *Rock Mechanics. Volume 1: Theoretical Fundamentals*, Technip, Paris.

Charlez, Ph.A. and Heugas, O. (1992) Measurement of Thermo-poroelastic Properties of Rocks: Theory and Applications. *Rock Characterization. ISRM Symposium: Eurock'92*, 14-17 September 1992, Chester, UK, edited by J.A. Hudson, London.

Coussy, O. (1994) *Mechanics of Porous Continua.* John Wiley and Sons Ltd., Chichester.

Coussy, O. (2004) *Poromechanics*, John Wiley and Sons Ltd., Chichester.

Couvreur, J.F., Thimus, J.F. and Lousberg, E. (1998) A Conceptual Model for Correlating Ultrasonic Attenuation to Deformational Behavior. *Paper SPE/ISRM 47347.*

Engstrøm, F. (1992) Rock Mechanical Properties of Danish North Sea Chalk. *Fourth North Sea Chalk Symposium*, Deauville, France, 21-23 September 1992.

Fjær, E., Holt, R.M., Horsrud, P., Raaen, A.M. and Risnes, R. (1992) *Petroleum Related Rock Mechanics*. Elsevier, Amsterdam.

Gaviglio, P. and Carrio, E. (1993) Contexte géologique et variations des propriétés physiques d'un calcaire tendre. *Geotechnical Engineering of Hard Soils - Soft Rocks*, Anagnostopoulos *et al.* (eds), Balkema, Rotterdam.

Gourri, A. (1991) Contribution à l'étude de l'influence des conditions de drainage sur les propriétés poroélastiques des roches carbonatées. *PhD Thesis*, Université Joseph Fourier de Grenoble (in french).

Homand, S. and Shao, J.F. (2000a) Mechanical Behaviour of a Porous Chalk and Water/Chalk Interaction. Part I: Experimental Study. *Oil & Gas Science and Technology - Revue de l'IFP*, **55**, 6, 591-598.

Homand, S. and Shao, J.F. (2000b) Mechanical Behaviour of a Porous Chalk and Water/Chalk Interaction. Part II: Numerical Modelling. *Oil & Gas Science and Technology - Revue de l'IFP*, **55**, 6, 2000, 599-609.

Keaney, G.M.J., Meredith, P.G. and Murell, S.A.F. (1998) Laboratory Study of Permeability Evolution in a "Tight" Sandstone under Non-Hydrostatic Stress Conditions. *Paper SPE/ISRM 47265.*

Larsen, I., Fjær, E., Renlie, L. and Zheng, Z. (1998) The Effects of Porosity and Stress on Dilatancy in Sandstone. *Paper SPE/ISRM 47199.*

Lin, W. (1981) Mechanical Behavior of Mesaverde Shale and Sandstone at High Pressure. *Paper SPE/DOE 9835*.

Longuemare, P., Schneider, F. and Onaisi, A. (1996) Study of the Behaviour of a Petroleum Reservoir During Depletion Using an Elasto-Plastic Constitutive Model. *Eurock'96*, Barla Ed., Balkema, 875-881.

Matà, C (2001) Etude expérimentale et modélisation mécanique des effets du balayage à l'eau dans une craie saturée d'huile - Application à l'industrie pétrolière. *PhD Thesis*, École Nationale des Ponts et Chaussées (in french).

Nicholson, E.D., Goldsmith, G. and Cook, J.M. (1998) Direct Observation and Modeling of Sand Production Processes in Weak Sandstone. *Paper SPE/ISRM 47328.*

Poutet, J., Manzoni, D., Hage-Chehade, F., Jacquin, C., Boutéca M., Thovert, J.F. and Adler, P.M. (1996) The Effective Mechanical Properties of Random Porous Media. *J. Mech. Phys. Solids*, **44**, 10, 1587-1620.

Rhett, D.W. and Teufel, L.W. (1992) Failure Criteria for High Porosity North Sea Chalk. *Fourth North Sea Chalk Symposium*, Deauville, France, 21-23 September 1992.

Sanchez-Palencia, E. (1980) *Non Homogeneous Media and Vibration Theory*. Springer, Berlin.

Schutjens, P.M.T.M. and de Ruig, H. (1996) The Influence of Stress Path and Permeability of an Overpressurised Reservoir Sandstone: Some Experimental Data. *Phys. Chem. Earth*, **22**, 1-2, 97-103.

Schutjens, P.M.T.M., Blanton, T.L., Martin, J.W., Lehr, B.C. and Baaijens, M.N. (1998) Depletion-Induced Compaction of an Overpressurised Reservoir Sandstone: an Experimental Approach. *Paper SPE 47277.*

Vincké, O. and Boutéca, M. (1992) An Estimation of Terminal Bulk Moduli of Sandstones Using their Petrographic and Petrophysic Description. *Structure et comportement mécanique des géomatériaux, colloque René Houpert.* Nancy, France, 10-11 Septembre 1992, Comptes rendus, F. Homand *et al.* eds., 27-36.

Vincké, O. (1994) An Estimation of Bulk Moduli of Sandstones as a Function of Confining Pressure Using their Petrographic and Petrophysic description. *Paper SPE/ISRM 28038.*

Vincké, O., Boutéca, M.J., Piau, J.M. and Fourmaintraux, D. (1998) Study of the Effective Stress at Failure. *Biot Conference on Poromechanics*, Louvain-La-Neuve, Belgique, 14-16 September 1998. A. A. Balkema, Rotterdam, 635-639.

Walsh, J.B. and Grosenbaugh, M.A. (1979) A New Model for Analyzing the Effect of Fractures on Compressibility. *Journal of Geophysical Research*, **84**, B7, 3532-3536.

Watt, P., Davies, G.F. and O' Connel, R. (1976) The Elastic Properties of Composites Material. *Review of Geophysics and Space Physics*, **14**, 4, 541-563.

Wissler, T.M. and Simmons, G. (1985) The Physical Properties of a Set of Sandstones - Part II: Permanent and Elastic Strains During Hydrostatic Compression to 200 MPa. *Int. J. Rock. Mech. Min. Sci. & Geomech. Abstr.*, **22**, 6, 393-406.

Wilkens, R., Simmons, G., Wissler, T.M. and Caruso, L. (1986) The Physical Properties of a Set of Sandstones - Part III: The Effects of Fined-grained Pore-filling Material on Compressional Wave Velocity. *Int. J. Rock. Mech. Min. Sci. & Geomech. Abstr.*, **23**, 4, 313-325.

Wong, T.F., David, C. and Zhu, W. (1997) The Transition from Brittle to Cataclastic Flow: Mechanical Deformation. *Journal of Geophysical Research*, **102**, B2, Feb. 10, 3009-3025.

Yale, D.P. and Crawford, B. (1998) Plasticity and Permeability in Carbonates: Dependance on Stress Path and Porosity. *Paper SPE/ISRM 47582.*

Zhang, J., Rai, C.S. and Sondergeld, C. (1998) Mechanical Strength of Reservoir Material: Key Information for Sand Prediction. *Paper SPE/ISRM 47365.*

Zhu, W. and Wong, T.F. (1997) The Transition from Brittle to Cataclastic Flow: Permeability Evolution. *Journal of Geophysical Research*, 102, B2, Feb. 10, 3027-3041.

Final manuscript received in May 2004

Copyright © 2004, Institut français du pétrole

Permission to make digital or hard copies of part or all of this work for personal or classroom use is granted without fee provided that copies are not made or distributed for profit or commercial advantage and that copies bear this notice and the full citation on the first page. Copyrights for components of this work owned by others than IFP must be honored. Abstracting with credit is permitted. To copy otherwise, to republish, to post on servers, or to redistribute to lists, requires prior specific permission and/or a fee. Request permission from Documentation, Institut français du pétrole, fax. +33 1 47 52 70 78, or revueogst@ifp.fr.